HAL
open science

Dynamo-based limit to the extent of a stable layer atop Earth's core

Thomas Gastine, Julien Aubert, Alexandre Fournier

To cite this version:

Thomas Gastine, Julien Aubert, Alexandre Fournier. Dynamo-based limit to the extent of a stable layer atop Earth's core. Geophysical Journal International, 2020, 222 (2), pp.1433 - 1448. 10.1093/gji/ggaa250 . insu-02878730

HAL Id: insu-02878730
https://insu.hal.science/insu-02878730v1

Submitted on 23 Jun 2020

HAL is a multi-disciplinary open access archive for the deposit and dissemination of scientific research documents, whether they are published or not. The documents may come from teaching and research institutions in France or abroad, or from public or private research centers.

L'archive ouverte pluridisciplinaire **HAL**, est destinée au dépôt et à la diffusion de documents scientifiques de niveau recherche, publiés ou non, émanant des établissements d'enseignement et de recherche français ou étrangers, des laboratoires publics ou privés.

Geophysical Journal International

Geophys. J. Int. (2020) **222,** 1433–1448
Advance Access publication 2020 May 20
GJI Geomagnetism, Rock Magnetism and Palaeomagnetism

doi: 10.1093/gji/ggaa250

Dynamo-based limit to the extent of a stable layer atop Earth's core

Thomas Gastine, Julien Aubert and Alexandre Fournier

Institut de Physique du Globe de Paris, Sorbonne Paris Cité, Université Paris-Diderot, UMR 7154 *CNRS,* 1 *rue Jussieu, F*-75005 *Paris, France. E-mail: gastine@ipgp.fr*

Accepted 2020 May 15. Received 2020 May 7; in original form 2019 October 11

SUMMARY

The existence of a stably stratified layer underneath the core–mantle boundary (CMB) has been recently revived by corroborating evidences coming from seismic studies, mineral physics and thermal evolution models. Such a layer could find its physical origination either in compositional stratification due to the accumulation of light elements at the top or the core or in thermal stratification due to the heat flux becoming locally subadiabatic. The exact properties of this stably stratified layer, namely its size $\mathcal{H}_s$ and the degree of its stratification characterized by the Brunt–Väisälä frequency N, are however uncertain and highly debated. A stable layer underneath the CMB can have crucial dynamical impacts on the geodynamo. Because of the inhibition of the convective motions, a stable layer is expected to primarily act as a low-pass filter on the magnetic field, smoothing out the rapidly varying and small-scale features by skin effect. To investigate this effect more systematically, we compute 70 global geodynamo models varying the size of the stably stratified layer from 0 to 300 km and its amplitude from $N/\Omega = 0$ to $N/\Omega \simeq 50$, Ω being the rotation rate. We show that the penetration of the convective flow in the stably stratified layer is controlled by the typical size of the convective eddies and by the local variations of the ratio N/Ω. Using quantitative measures of the degree of morphological semblance between the magnetic field obtained in numerical models and the geomagnetic field at the CMB, we establish an upper bound for the stable layer thickness $\mathcal{H}_s < (N/\Omega)^{-1}\mathcal{L}_s$, $\mathcal{L}_s$ being the horizontal size of the convective flow at the base of the stable layer. This defines a strong geomagnetic constraint on the properties of a stably stratified layer beneath the CMB. Unless unaccounted double-diffusive effects could drastically modify the dynamics of the stable layer, our numerical geodynamo models hence favour no stable stratification atop the core.

Key words: Composition and structure of the core; Core; Dynamo: theories and simulations; Numerical modelling.

1 INTRODUCTION

The convective motions that develop in Earth's liquid outer core are considered as the primary source of power to sustain the geomagnetic field via dynamo action. This results from the combination of thermal and compositional buoyancy sources. The Earth secular cooling and the latent heat release due to the solidification of iron at the inner core boundary (ICB) provide the thermal heat sources, while the expulsion of light elements from the iron-rich inner core into the fluid outer core constitutes another source of buoyancy of compositional origin (e.g. Lister & Buffett 1995).

The exact convective state of the Earth liquid core is however uncertain. The usual assumption posits that the outer core is entirely convective, well-mixed by the turbulent convective motions. This hypothesis has been however questioned by seismic studies that rather suggest the presence of inhomogeneous layers above the ICB (e.g. Souriau & Poupinet 1991) or below the core–mantle boundary (CMB) (e.g. Tanaka 2007; Helffrich & Kaneshima 2010; Kaneshima 2018). Those layers could arise because of stable stratification of thermal or compositional origin. The degree of stratification can be quantified by the Brunt–Väisälä frequency expressed by

$$N^2 = -\frac{g}{\rho}\frac{\partial \rho}{\partial r} - \frac{\rho g^2}{K_S}, \tag{1}$$

where g is the gravity, K_S the isentropic bulk modulus and ρ the fluid density. The possible stable layer underneath the CMB has been recently the focus of a large array of studies that span various scientific fields encompassing seismic studies, mineral physics and geomagnetic analyses (for a review, see Hirose *et al.* 2013).

On the seismology side, several studies, based on the analysis of traveltimes of SmKS waves, report P-wave velocities between 0.1 and 1 per cent slower than PREM at the top of the core. They attribute this deviation to an inhomogeneous stably stratified layer

© The Author(s) 2020. Published by Oxford University Press on behalf of The Royal Astronomical Society.

Downloaded from https://academic.oup.com/gji/article-abstract/222/2/1433/5841194 by Biblio Planets user on 23 June 2020

which would yield a mean density profile that would significantly depart from the adiabat. The inferred thickness $\mathcal{H}_s$ of this layer has evolved from $\mathcal{H}_s \sim 100$ km in earlier studies (e.g. Lay & Young 1990; Tanaka 2007) to larger values ranging from 300 to 450 km in more recent analyses (Helffrich & Kaneshima 2010; Kaneshima & Matsuzawa 2015; Tang *et al.* 2015; Kaneshima 2018). The evaluation of the associated Brunt–Väisälä frequency is always delicate since it directly depends on the chemical composition of the core (e.g. Brodholt & Badro 2017) but tentative estimates yield $N \sim 0.5-1$ mHz (Helffrich & Kaneshima 2010). There is, however, no consensus on the interpretation of these seismic observations, and some seismic studies rather favour no stratification at the top of the core (e.g. Alexandrakis & Eaton 2010; Irving *et al.* 2018). Irving *et al.* (2018) for instance explain the deviations to PREM by a refined equation of state that yields steeper density profiles close to the CMB.

Stable stratification of thermal origin arises when the temperature gradient becomes subadiabatic. This directly depends on the heat flux at the CMB and on the outer core thermal conductivity. The latter has been the subject of intense debates over the recent years. *Ab-initio* first principle numerical calculations yield conductivity values ranging from 100 to 150 $\mathrm{W\,m^{-1}\,K^{-1}}$ (de Koker *et al.* 2012; Pozzo *et al.* 2012, 2013) significantly larger than previous estimate of 30 $\mathrm{W\,m^{-1}\,K^{-1}}$ (Stacey & Loper 2007). On the other hand, high-pressure experiments yield contradictory results: while some are supportive of the *ab initio* findings (Gomi *et al.* 2013; Ohta *et al.* 2016), others rather favour the lower previously accepted conductivity value (Konôpková *et al.* 2016). A CMB heat flux of roughly $Q_{\mathrm{CMB}} = 15$ TW would be required to accommodate a fully convective core for the highest thermal conductivities. Although estimates of the actual heat flux at the CMB are rather uncertain (e.g. Lay *et al.* 2008), $Q_{\mathrm{CMB}} = 15$ TW certainly lies in the high range of commonly accepted values. Stable thermal stratification below the CMB is hence the favoured scenario (Pozzo *et al.* 2012; Gomi *et al.* 2013), would the actual core conductivity lies in the current high-range estimate.

Geomagnetic observations provide another source of constraints on the physical properties of a stable layer underneath the CMB, since this layer would damp radial motions and/or harbour waves for which gravity would act as a restoring force. The geomagnetic secular variation (SV) is governed for the most part by fluid flow at the top of the core. The presence of a stably stratified layer underneath the CMB implies that the radial velocity is weaker than the horizontal components. Using arguments based on a careful analysis of the Navier–Stokes equations under the tangentially geostrophic and Boussinesq approximations in a stratified layer, Jault & Le Mouël (1991) showed that the corresponding flow is not strictly toroidal, as its large-scale components can be partly poloidal. In short, even if the radial flow is much smaller than the horizontal one, its radial gradient can not be neglected against the horizontal divergence of the flow for the large scales of motion. In that sense, trying to establish that the core is stratified considering purely toroidal core surface flow for the analysis of the SV may be overkill, especially when one is restricted to analyse the large scales of motion. Accordingly, Lesur *et al.* (2015) found that a large-scale core surface flow permitting up- and downwellings was more adapted to account for the secular variation during the magnetic satellite era than its strictly toroidal equivalent precluding radial flow underneath the CMB. The latter hypothesis led typically to a 15 per cent increase in the root-mean-squared misfit to low-latitude satellite data compared to the misfit obtained with the former. There are regions at the core surface (for instance underneath the Indian Ocean), where some radial flow is mandatory to account for the data (e.g. Amit 2014; Baerenzung *et al.* 2016). That does not mean that there is no stratified layer, it simply implies that SV data alone do not have a real resolving power on the properties of a hypothetical stratified layer at the top of core. In fact, in this study we shall stress that much stronger constraints are obtained by studying the morphology of the magnetic field at the top of the core. With regard to wave motion, Braginsky (1993) hypothesized that the decadal variations of the magnetic field could be related to the excitation of MAC waves in a stable layer with $\mathcal{H}_s = 80$ km and $N \sim \Omega$, Ω being Earth's rotation rate. This idea was more recently revisited by Buffett (2014) who attributes the 60 yr period observed in the secular variation of the axisymmetric dipole to MAC waves. Best-fitting linear models yield $\mathcal{H}_s = 130 - 140$ km and $N = 0.74 - 0.84\,\Omega$ (Buffett *et al.* 2016), a degree of stratification much weaker than the estimates coming from seismic studies. In practice, the reference models are assumed to be spherically symmetric and yield a function $N(r)$. Table 1 lists selected publications which provide estimates of $\mathcal{H}_s$ and N_m/Ω, with $N_m = \max_r N(r)$.

Table 1. Selected publications that propose values for the physical properties of the stably-stratified layer underneath the CMB using $\Omega = 7.29 \times 10^{-5}\ \mathrm{s}^{-1}$.

Reference	Name	$\mathcal{H}_s$ (km)	N_m/Ω
Braginsky (1993)	B93	80	2
Buffett & Seagle (2010)	BS11	70	55
Helffrich & Kaneshima (2010)	HK10	300	7–14.7
Gubbins & Davies (2013)	GD13	100	20.6
Buffett *et al.* (2016)	BKH16	130–140	0.74–0.84
Irving *et al.* (2018)	ICL18	0	$\simeq 0$

In this study, we aim to analyse the physical influence of a stable layer below the CMB by means of 3-D global geodynamo models. Takehiro & Lister (2001) analysed the propagation of thermal Rossby waves in presence of a stably stratified temperature gradient in the limit of an inviscid fluid. They showed that the distance of penetration $\mathcal{D}_p$ of a convective eddy of size $\mathcal{L}_s$ is inversely proportional to the ratio of the Brunt–Väisälä and the rotation frequencies

$$\mathcal{D}_p \sim \left(\frac{N}{\Omega}\right)^{-1} \mathcal{L}_s\,. \tag{2}$$

Hence, the larger the ratio N/Ω, the smaller the penetration distance. The above theoretical scaling can be seen as the result of two competing linear physical effects: on the one-hand rapid-rotation goes along with quasi bi-dimensional Taylor columns aligned with the rotation axis, while on the other hand the stable stratification promotes motions in horizontal planes perpendicular to the radial stratification. Subsequent analyses by Takehiro (2015) have however questioned the validity of this hydrodynamic scaling relation in presence of a magnetic field. Based on the penetration distance of Alfvén waves, he instead suggests that the above hydrodynamic scaling could be replaced by

$$\frac{\mathcal{D}_p}{d} \sim \frac{\omega_A}{\omega_{\mathrm{diss}}}\,, \tag{3}$$

where ω_A is the typical frequency of the Alfvén waves, ω_{diss} is a diffusion frequency resulting from the average between kinematic and magnetic diffusivities and d is the extent of the fluid domain. However, the validity of the above linear scaling has only been tested by Takehiro & Sasaki (2018b) in the context of non-linear models of rotating convection in presence of an imposed background magnetic field. Global 3-D numerical simulations of stellar (Brun *et al.* 2017) and planetary (Dietrich & Wicht 2018)

Downloaded from https://academic.oup.com/gji/article-abstract/222/2/1433/5841194 by Biblio Planets user on 23 June 2020

convection in spherical shells under the anelastic approximation have shown little support for the hydrodynamic scaling (2). This is likely because of the important role played by inertia in these numerical computations where rotation has a moderate influence on the convective flow (e.g. Zahn 1991; Hurlburt *et al.* 1994). Geodynamo models that incorporate a stable layer are either limited to moderate degrees of stratification $N/\Omega < 5$ (Olson *et al.* 2017; Yan & Stanley 2018; Christensen 2018) or to weakly supercritical convection (Nakagawa 2015), hence restricting further tests of the relevance of the above scalings. The first goal of the present study is precisely to estimate the penetration distance in rapidly rotating geodynamo models to assess the validity of eqs (2) and (3).

Numerical dynamo models have also shown that stable layers can have a strong impact on the magnetic field. In the limit of vanishing penetrative convection, a stably stratified region can be roughly approximated by a stagnant conducting fluid layer. The magnetic field parts which vary rapidly with time are then strongly damped by the magnetic skin effect. In the context of modelling Mercury's dynamo, Christensen (2006) has for instance shown that the magnetic field atop a stable layer becomes more dipolar and more axisymmetric (see also Gubbins 2007; Christensen & Wicht 2008; Stanley & Mohammadi 2008; Takahashi *et al.* 2019). The second objective of this study consists in quantifying the influence of a stable layer on the magnetic field morphology at the CMB. To assess the agreement between the numerical models fields and the geomagnetic field at the CMB, we resort to using the four rating parameters introduced by Christensen *et al.* (2010).

To meet these main objectives, we conduct a systematic parameter study varying $\mathcal{H}_s$ from 0 to 290 km and N_m/Ω from 0 to more than 50 for different combinations of Ekman, Rayleigh and magnetic Prandtl numbers. This work complements previous studies on the same topic that have assumed weaker stratification degrees $N_m/\Omega < 5$ (Olson *et al.* 2017; Yan & Stanley 2018; Christensen 2018).

The paper is organized as follows. The details of the numerical geodynamo model and the control parameters are introduced in Section 2. Section 3 presents the numerical results, while Section 4 describes the geophysical implications. We conclude with a summary of our findings in Section 5.

2 DYNAMO MODEL

2.1 Model equations and control parameters

We consider a spherical shell of inner radius r_i and outer radius r_o filled with an incompressible conducting fluid of constant density ρ which rotates at a constant frequency Ω about the z-axis. We adopt a dimensionless formulation of the magneto-hydrodynamic equations under the Boussinesq approximation. In the following, we use the shell thickness $d = r_o - r_i$ as the reference length scale and the viscous diffusion time d^2/ν as the reference time scale. Velocity is expressed in units of ν/d and magnetic field in units of $\sqrt{\rho\mu\lambda\Omega}$, where μ is the magnetic permeability, ν is the kinematic viscosity and λ is the magnetic diffusivity. The temperature scale is defined using the value of the gradient of the background temperature T_c at the inner boundary $|\mathrm{d}T_c/\mathrm{d}r|_{r_i}$ multiplied by the lengthscale d.

The dimensionless equations that control the time evolution of the velocity u, the magnetic field $\boldsymbol{B}$ and the temperature perturbation ϑ are then expressed by

$$\nabla \cdot \boldsymbol{u} = 0\,, \quad \nabla \cdot \boldsymbol{B} = 0\,, \tag{4}$$

$$\frac{\partial \boldsymbol{u}}{\partial t} + \boldsymbol{u}\cdot\nabla\boldsymbol{u} + \frac{2}{E}\boldsymbol{e}_z \times \boldsymbol{u} = -\nabla p + \frac{Ra}{Pr} g\,\vartheta\,\boldsymbol{e}_r + \frac{1}{E\,Pm}(\nabla\times\boldsymbol{B})\times\boldsymbol{B} + \nabla^2\boldsymbol{u}\,, \tag{5}$$

$$\frac{\partial B}{\partial t} = \nabla\times(\boldsymbol{u}\times\boldsymbol{B}) + \frac{1}{Pm}\nabla^2\boldsymbol{B}\,, \tag{6}$$

$$\frac{\partial \vartheta}{\partial t} + \boldsymbol{u}\cdot\nabla\vartheta + u_r\frac{\mathrm{d}T_c}{\mathrm{d}r} = \frac{1}{Pr}\nabla^2\vartheta\,, \tag{7}$$

where p is the pressure, $\boldsymbol{e_r}$ is the unit vector in the radial direction and $g = r/r_o$ is the dimensionless gravity profile. The dimensionless set of eqs (4)–(7) is governed by four dimensionless control parameters, namely the Ekman number E, the Rayleigh number Ra, the Prandtl number Pr and the magnetic Prandtl number Pm defined by

$$E = \frac{\nu}{\Omega d^2},\; Ra = \frac{\alpha g_o d^4}{\nu\kappa}\left|\frac{\mathrm{d}T_c}{\mathrm{d}r}\right|_{r_i},\; Pr = \frac{\nu}{\kappa},\; Pm = \frac{\nu}{\lambda}\,, \tag{8}$$

where α is the thermal expansivity, g_o is the gravity at the outer boundary and κ is the thermal diffusivity.

The location and the degree of stratification of the stable layer are controlled by the radial variations of the gradient of the temperature background $\mathrm{d}T_c/\mathrm{d}r$. In regions where $\mathrm{d}T_c/\mathrm{d}r < 0$, the flow is indeed convectively unstable, while stably stratified regions correspond to $\mathrm{d}T_c/\mathrm{d}r > 0$. We adopt here a simplified parametrized background temperature gradient to easily vary the location and the amplitude of the stably stratified region.

To do so, one possible approach, introduced by Takehiro & Lister (2001), consists in assuming an homogeneous volumetric heat source in the convectively unstable region and a constant positive temperature gradient $\mathrm{d}T_c/\mathrm{d}r$ in the stably stratified outer layer. A continuous profile is then obtained by introducing a smooth tanh function centred at the transition radius r_s. This approach has the disadvantage of introducing an additional parameter σ which controls the stiffness of the transition between the two layers (e.g. Nakagawa 2011, 2015).

A possible way out to remove the ambiguity of defining a suitable value for σ consists in rather assuming that the degree of stratification grows linearly with radius across the stably stratified layer (e.g. Rieutord 1995; Lister & Buffett 1998; Buffett 2014; Vidal & Schaeffer 2015; Buffett *et al.* 2016). In this case, the maximum degree of stratification is reached at the CMB and linearly decreases to zero at the top of the convective part, in broad agreement with some seismic studies (e.g. Helffrich & Kaneshima 2013). The temperature background $\mathrm{d}T_c/\mathrm{d}r$ is now entirely specified by the transition radius r_s and the maximum degree of stratification Γ. In the following, we adopt a piecewise function defined by

$$\frac{\mathrm{d}T_c}{\mathrm{d}r} = \begin{cases} -1, & r < r_s\,, \\ \Gamma\dfrac{r-r_s}{\mathcal{H}_s} + \dfrac{r-r_o}{\mathcal{H}_s}, & r \geq r_s\,, \end{cases} \tag{9}$$

where $\mathcal{H}_s = r_o - r_s$ corresponds to the thickness of the stable layer. The control parameter Γ is related to the value of the Brunt–Väisälä frequency at the CMB N_m via

$$\frac{N_m}{\Omega} = \sqrt{\frac{Ra\,E^2}{Pr}\,\Gamma}\,. \tag{10}$$

The set of eqs (4)–(7) is supplemented by boundary conditions. We assume here rigid mechanical boundaries at both the ICB and

Downloaded from https://academic.oup.com/gji/article-abstract/222/2/1433/5841194 by Biblio Planets user on 23 June 2020

the CMB. We use mixed thermal boundary conditions with

$$\vartheta|_{r=r_i} = 0, \quad \left.\frac{\partial \vartheta}{\partial r}\right|_{r=r_o} = 0\,.$$

This choice of thermal boundary conditions grossly reflects a fixed solidification temperature at the inner core boundary and a fixed flux extracted by the mantle at the CMB. The magnetic field is matched to a potential field at the outer boundary, while the inner core is treated as an electrically conducting rigid sphere which is free to rotate about the z-axis.

2.2 Numerical method

The majority of the simulations computed in this study have been carried out using the open-source code `MagIC` (Wicht 2002, freely available at https://github.com/magic-sph/magic), while some complementary simulations were integrated using the `PARODY-JA` code (Dormy *et al.* 1998; Aubert *et al.* 2008).

The set of eqs (4–7) is solved in the spherical coordinates (r, θ, ϕ) by expanding the velocity and the magnetic fields into poloidal and toroidal potentials

$$\boldsymbol{u} = \nabla \times (\nabla \times W\,\boldsymbol{e_r}) + \nabla \times Z\,\boldsymbol{e_r}\,,$$
$$\boldsymbol{B} = \nabla \times (\nabla \times G\,\boldsymbol{e_r}) + \nabla \times H\,\boldsymbol{e_r}\,.$$

The unknowns W, Z, G, H, ϑ and p are expanded in spherical harmonic functions up to degree $\ell_{\max}$ in the angular directions. In the radial direction, `MagIC` uses a Chebyshev collocation method with N_r radial gridpoints r_k defined by

$$r_k = \frac{1}{2}(x_k + r_o + r_i),\ x_k = \cos\left[\frac{(k-1)\pi}{N_r - 1}\right],$$

for $k \in [1, N_r]$, while `PARODY-JA` adopts a second-order finite difference scheme with N_r grid points. For both codes, the equations are advanced in time using an implicit-explicit Crank-Nicolson second-order Adams–Bashforth scheme, which treats the nonlinear terms and the Coriolis force explicitly and the remaining terms implicitly. The advection of the background temperature gradient $u_r\,\mathrm{d}T_c/\mathrm{d}r$ is handled implicitly when $N > \Omega$ to avoid severe time step limitations that would otherwise occur because of the propagation of gravity waves (for a comparison, see Brown *et al.* 2012). Glatzmaier (1984), Tilgner & Busse (1997) or Christensen & Wicht (2015) provide a more comprehensive description of the numerical method and the spectral transforms involved in the computations. In both `MagIC` and `PARODY-JA`, the spherical transforms are handled using the open-source library `SHTns` (Schaeffer 2013, freely available at https://bitbucket.org/nschaeff/shtns)

Standard Chebyshev collocation points such as the Gauss–Lobatto nodal points x_k feature a typical grid spacing that decays with N_r^{-2} close to the boundaries. In presence of a sizeable magnetic field, this imposes severe time step restrictions due to the propagation of Alfvén waves in the vicinity of the boundaries (e.g. Christensen *et al.* 1999). To alleviate this limitation, we adopt in `MagIC` the mapping from Kosloff & Tal-Ezer (1993) defined by

$$y_k = \frac{\arcsin(\alpha_{\text{map}}\,x_k)}{\arcsin(\alpha_{\text{map}})},\ k = 1, \cdots, N_r$$

where $0 \le \alpha_{\text{map}} < 1$ is the mapping coefficient. This mapping allows a more even redistribution of the radial grid points (see Boyd 2001, section 16.9). To maintain the spectral convergence of the radial scheme, the mapping coefficient α_{map} has to be kept under a threshold value defined by

$$\alpha_{\text{map}} \le \left[\cosh\left(\frac{|\ln\epsilon|}{N_r - 1}\right)\right]^{-1}$$

where ϵ is the machine precision. Comparison of simulations with or without this mapping shows an increased average time-step size by a factor of two.

2.3 Parameters choice and diagnostics

A systematic parameter study has been conducted varying the Ekman number between $E = 3 \times 10^{-4}$ and $E = 10^{-6}$, the Rayleigh number between $Ra = 3 \times 10^6$ and $Ra = 9 \times 10^{10}$ and the magnetic Prandtl number within the range $0.5 < Pm < 5$. For all the numerical models, Pr is kept fixed to 1. The influence of the stable layer has been studied by varying its degree of stratification within the range $0 \le N_m/\Omega < 52$ and its thickness using the following values $\mathcal{H}_s \in [0, 53, 87, 155, 200, 290]$ km. Throughout the paper, the conversion between dimensionless and dimensional lengthscales is obtained by assuming $d = 2260$ km. To ensure a good statistical convergence, the numerical models have been integrated for at least half a magnetic diffusion time τ_λ, except for the simulation with $E = 10^{-6}$ which has been integrated over $0.2\,\tau_\lambda$. In total, 70 direct numerical simulations detailed in Table A1 have been computed in this study.

In the following, we use overbars to denote time averages and angular brackets to express volume averages:

$$\langle f \rangle = \frac{1}{V}\int_V f\,\mathrm{d}V, \quad \overline{f} = \frac{1}{\tau}\int_{t_o}^{t_o+\tau} f\,\mathrm{d}t,$$

where V is the spherical shell volume, t_o is the starting time for averaging and τ is the time-averaging period. The integration over a spherical surface is expressed by

$$\langle f \rangle_s = \int_0^{\pi}\int_0^{2\pi} f(r,\theta,\phi)\sin\theta\,\mathrm{d}\theta\,\mathrm{d}\phi\,.$$

The typical flow amplitude is expressed by the magnetic Reynolds number Rm defined by

$$Rm = \overline{\langle u^2 \rangle^{1/2}}\,Pm\,, \tag{11}$$

while the mean magnetic field amplitude is given by the Elsasser number Λ

$$\Lambda = \overline{\langle B^2 \rangle}\,. \tag{12}$$

To characterize the typical convective flow lengthscale, we introduce the mean spherical harmonic degree at the radius r

$$\bar{\ell}(r) = \frac{\overline{\sum_\ell \ell\, u_\ell^2(r)}}{\overline{\sum_\ell u_\ell^2(r)}},$$

and the corresponding lengthscale

$$\mathcal{L}(r) = \frac{\pi\, r}{\bar{\ell}(r)},$$

where $u_\ell^2(r)$ corresponds to the kinetic energy content at the spherical harmonic degree ℓ and at the radius r (Christensen & Aubert 2006). In the following we will mainly focus on the convective flow lengthscale at the transition between the stably-stratified outer layer and the inner convective core, denoted by

$$\mathcal{L}_s = \frac{\pi\, r_s}{\bar{\ell}_s}, \quad \bar{\ell}_s = \bar{\ell}(r = r_s)\,. \tag{13}$$

Downloaded from https://academic.oup.com/gji/article-abstract/222/2/1433/5841194 by Biblio Planets user on 23 June 2020

The morphological agreement between the magnetic fields produced in the numerical models and the geomagnetic field is assessed by four criteria introduced by Christensen *et al.* (2010). This involves physical quantities defined using the spectral properties of the magnetic field at the CMB for spherical harmonic degree and order lower than 8. The ratio of power between the axial dipole and the non-dipolar contributions defines the parameter AD/NAD. The degree of equatorial symmetry of the CMB field is measured by the parameter O/E, while the ratio of power between the axisymmetric and the non-axisymmetric contributions for the non-dipolar field is given by Z/NZ. Finally, the magnetic flux concentration factor FCF is defined by the variance of the square of the radial component of the magnetic field at the CMB. The combination of the time-average of these four quantities allow to estimate the degree of compliance χ^2 between the numerical model field and the geomagnetic field (see Christensen *et al.* 2010, for the details).

Table A1 summarizes the values of the main diagnostics for all the simulations computed in this study.

3 RESULTS

3.1 Penetrative rotating convection

A stably stratified layer lying above a convective region does not act as a simple rigid wall that would quench all convective motions. In practice, the parcels of fluid which are moving outward in the vicinity of the interface rather penetrate over some distance $\mathcal{D}_p$ into the stably stratified layer, gradually loosing their momentum. An easy and practical way to visualize this phenomenon (e.g. Rogers & Glatzmaier 2005) resorts to looking at the radial profile of poloidal kinetic energy averaged over time

$$E_p = \frac{1}{2}\sum_{\ell,m} \ell(\ell+1)\left[\frac{\ell(\ell+1)}{r^2}\overline{|W_{\ell m}|^2} + \overline{\left|\frac{\mathrm{d}W_{\ell m}}{\mathrm{d}r}\right|^2}\right], \tag{14}$$

where $W_{\ell m}$ is the poloidal potential at degree ℓ and order m. Fig. 1(a) shows the comparison of E_p for one fully convective model and for five simulations with $\mathcal{H}_s = 200$ km and an increasing degree of stratification N_m/Ω. All models exhibit comparable profiles in most of the convective core and only start to depart from each other in the upper part of the convective region. In the stably stratified outer layer, the poloidal energy content decreases with increasing values of N_m/Ω. While the simulation with $N_m/\Omega = 0.26$ is comparable to the fully convective model in this region, the case with the strongest stratification $N_m/\Omega = 51.96$ features an energy content roughly four orders of magnitude below its fully convective counterpart.

The radial profiles of E_p can be further used to estimate the distance of penetration $\mathcal{D}_p$ either by measuring the point where E_p drops below a given fraction of its maximum value (e.g. Rogers & Glatzmaier 2005), or by measuring the *e*-folding distance of E_p at the edge of the convective layer (e.g. Takehiro & Lister 2001). Both methods carry their own limitations: the former is very sensitive to the threshold value when E_p shows a stiff decay at the transition; while the latter can yield $\mathcal{D}_p$ larger than the actual thickness of the stably-stratified layer (see Dietrich & Wicht 2018, Fig. 10).

A complementary approach, which has proven to be insightful in the context of Solar convection (e.g. Browning *et al.* 2004; Deng & Xiong 2008; Brun *et al.* 2017), resorts to studying the radial variations of the convective flux or of the buoyancy power (see Takehiro & Sasaki 2018b) expressed by

$$\mathcal{P} = \frac{Ra\,E}{Pr}\, g\, \overline{\langle u_r \vartheta\rangle_s}\,. \tag{15}$$

Fig. 1(b) shows the radial profiles of $\mathcal{P}$ for the same numerical simulations as in Fig. 1(a). In the convective core, the eddies which are hotter (colder) than their surroundings are moving outward (inward), yielding a positive buoyancy power $\mathcal{P}$. But when a convective parcel overshoots in the subadiabatic layer, the positive radial velocity becomes anticorrelated with the negative thermal fluctuations, yielding $\mathcal{P} < 0$ at the base of the stably stratified layer (e.g. Takehiro & Sasaki 2018b). As shown in the inset of Fig. 1(b), the radial extent of the fluid region where $\mathcal{P} < 0$ is a decreasing function of N_m/Ω. Following Browning *et al.* (2004), the upper boundary of the overshooting region can be defined by the radius at which the buoyancy power attains 10 per cent of its minimum negative value

$$\mathcal{P}(r_p) = 0.1\,\min(\mathcal{P}) \quad \text{and} \quad r_p > r_{\min}, \tag{16}$$

where $r_{\min}$ corresponds to the radius where the buoyancy power reaches its minimum. This definition still involves an arbitrary threshold value, but r_p has been found by previous studies to be fairly insensitive to this (e.g. Brun *et al.* 2011). The location of r_p using this definition are marked by vertical segments in Fig. 1(b). We then define the penetration depth $\mathcal{D}_p$ by

$$\mathcal{D}_p = r_p - r_s\,. \tag{17}$$

The adopted definition of r_p guarantees that the penetration depth remains bounded by $\mathcal{H}_s$, that is $\max(\mathcal{D}_p) \leq \mathcal{H}_s$.

We now examine how $\mathcal{D}_p$ evolves with the degree of stratification N_m/Ω. In the physical regime of rapidly rotating convection and in absence of magnetic field, the linear stability analysis by Takehiro & Lister (2001) suggest that the distance of penetration is inversely proportional to the ratio of the Brunt–Väisälä and the rotation frequencies (eq. 2). It is however not entirely clear whether this scaling should still hold in presence of a magnetic field (Takehiro 2015).

Fig. 2(a) shows $\mathcal{D}_p$ as a function of $(N_m/\Omega)\bar{\ell}_s$ for all the numerical simulations computed in this study. For each stable layer thickness $\mathcal{H}_s$, the evolution of $\mathcal{D}_p$ with $(N_m/\Omega)\bar{\ell}_s$ is comprised of two parts: one nearly horizontal part where the degree of stratification is weak enough such that $\mathcal{D}_p \simeq \mathcal{H}_s$; and a second branch for $(N_m/\Omega)\bar{\ell}_s > 100$ where $\mathcal{D}_p$ decreases with the degree of stratification. However, a dependence to $\mathcal{H}_s$ is still visible in the decaying branch. At a fixed value of $(N_m/\Omega)\bar{\ell}_s$, the penetration distance can indeed vary by a factor of roughly two (see also Dietrich & Wicht 2018). We attribute this remaining dependence to the local radial variations of the Brunt–Väisälä frequency (eq. 9). Since the degree of stratification almost linearly increases from neutral stability at the edge of the convective layer to N_m/Ω at the CMB, a convective eddy that penetrates deep in the stable layer does not feel the same stratification as one that would hardly scratch into it. To account for this effect, we introduce an *effective stratification* $\mathcal{N}/\Omega$ defined by the averaged Brunt–Väisälä frequency between the spherical shell radii r_s and r_p

$$\left(\frac{\mathcal{N}}{\Omega}\right)^2 = \frac{Ra E^2}{Pr}\,\frac{\displaystyle\int_{r_s}^{r_p} g\,\frac{\mathrm{d}T_c}{\mathrm{d}r}\,r^2\mathrm{d}r}{\displaystyle\int_{r_s}^{r_p} r^2\mathrm{d}r}\,. \tag{18}$$

Fig. 2(b) shows $\mathcal{D}_p$ as a function of $(\mathcal{N}/\Omega)\bar{\ell}_s$. In contrast to Fig. 2(a), the measured penetration distances $\mathcal{D}_p$ now collapse on one single scaling behaviour. A best fit for the strongly stratified simulations

Downloaded from https://academic.oup.com/gji/article-abstract/222/2/1433/5841194 by Biblio Planets user on 23 June 2020

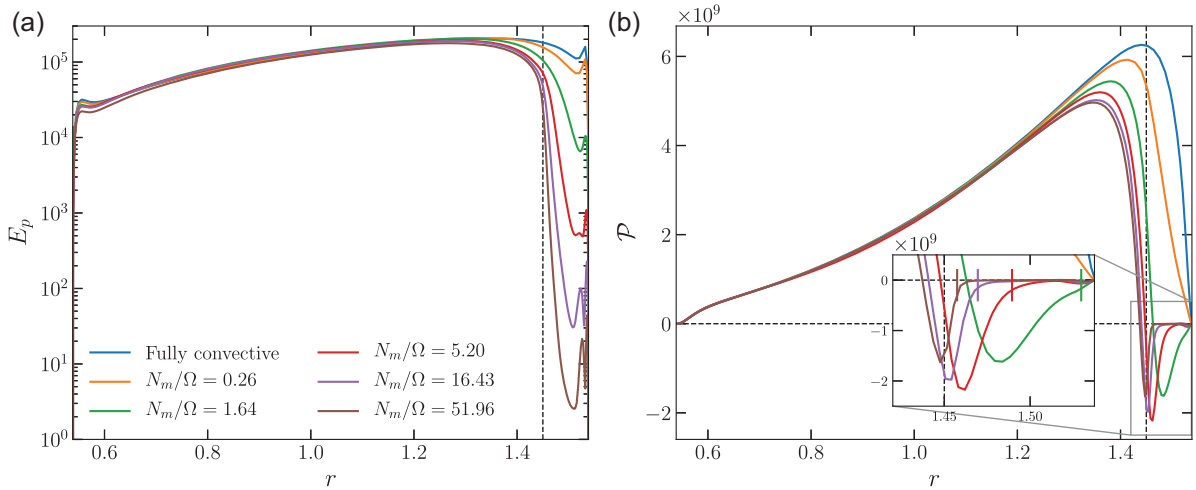

Figure 1. (a) Time-averaged poloidal kinetic energy (eq. 14) as a function of radius for numerical models with $E = 3 \times 10^{-5}$, $Ra = 3 \times 10^8$, $Pm = 2.5$, $r_s = 1.45$ ($\mathcal{H}_s = 200$ km) and different values of N_m/Ω. The vertical dashed line corresponds to $r = r_s$. (b) Time-averaged buoyancy power $\mathcal{P}$ (eq. 15) as a function of radius. The vertical dashed line corresponds to $r = r_s$, while the horizontal dashed line corresponds to the neutral buoyancy line $\mathcal{P} = 0$. The zoomed-in inset highlights the radial profiles of $\mathcal{P}$ in the stably stratified layer. The small coloured vertical segments mark the extent of the convective penetration r_p defined in eq. (16).

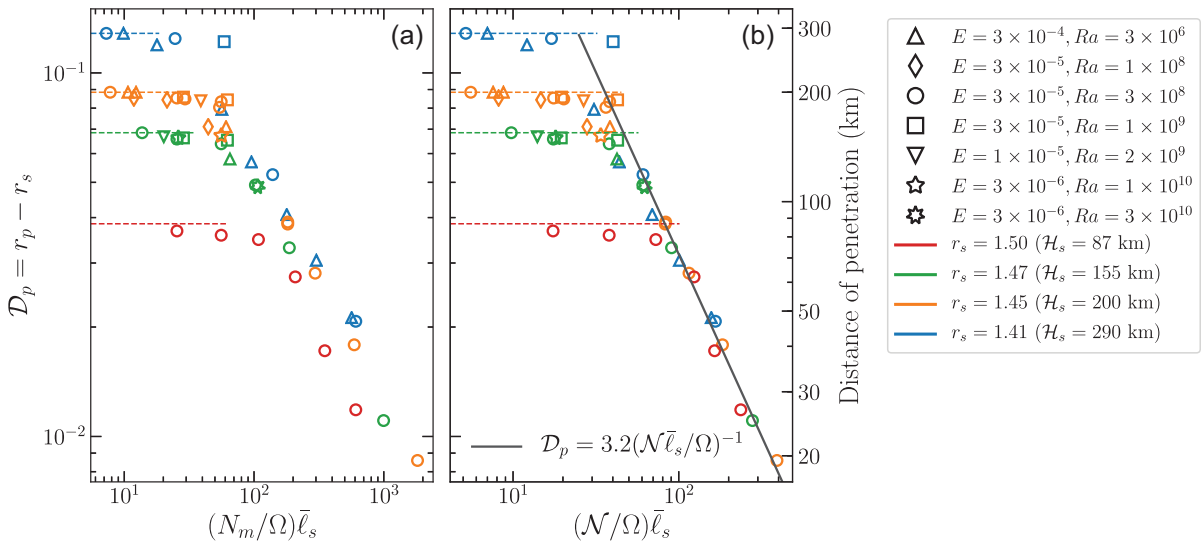

Figure 2. Distance of penetration of the convective flow $\mathcal{D}_p$ (eq. 17) as a function of $(N_m/\Omega)\,\bar{\ell}_s$ (left-hand panel) and as a function of $(\mathcal{N}/\Omega)\,\bar{\ell}_s$ (right-hand panel). The colour of the symbols correspond to the thickness of the stratified layer $\mathcal{H}_s$, while the shape correspond to different (E, Ra) combination of parameters listed in Table A1. In each panel, the coloured dashed lines correspond to the maximum extent of the penetration, that is $\mathcal{D}_p = \mathcal{H}_s$. The solid black in panel (b) line corresponds to a best fit for the models with $(\mathcal{N}/\Omega)\,\bar{\ell}_s > 80$.

with $(\mathcal{N}/\Omega)\,\bar{\ell}_s > 80$ yield

$$\mathcal{D}_p = (3.19 \pm 0.67)\left(\frac{\mathcal{N}}{\Omega}\bar{\ell}_s\right)^{-1.00\pm0.04} \tag{19}$$

in excellent agreement with the theoretical scaling (2) from Takehiro & Lister (2001).

Although this scaling has been theoretically derived in absence of magnetic field, the penetration distance of convective eddies in dynamo models is found to still only depend on the ratio of the local Brunt–Väisälä frequency to the rotation rate and on the typical horizontal size of the convective flow at the transition radius. This implies that at a given stratification degree, small scale eddies will penetrate over a shorter distance than the large ones. To illustrate this physical phenomenon, Fig. 3 shows snapshots of the radial component of the convective flow u_r for four numerical simulations with comparable N_m/Ω but decreasing Ekman numbers from $E = 3 \times 10^{-4}$ (a) to $E = 10^{-6}$ (d). The typical convective flow lengthscale in the upper part of the convective region decreases with the Ekman number and the penetration distance decreases accordingly. For the two cases with the lowest Ekman number, we observe a clear separation between larger flow lengthscales in the bulk of the convective core and smaller scale features at r_s. To quantify this scale separation, we thus introduce another lengthscale measure deeper in the convective region, denoted by

$$\mathcal{L}_b = \frac{\pi\, r_b}{\bar{\ell}_b}, \quad \bar{\ell}_b = \bar{\ell}(r = r_b)\,, \tag{20}$$

where $r_b = r_i + 0.25$.

Downloaded from https://academic.oup.com/gji/article-abstract/222/2/1433/5841194 by Biblio Planets user on 23 June 2020

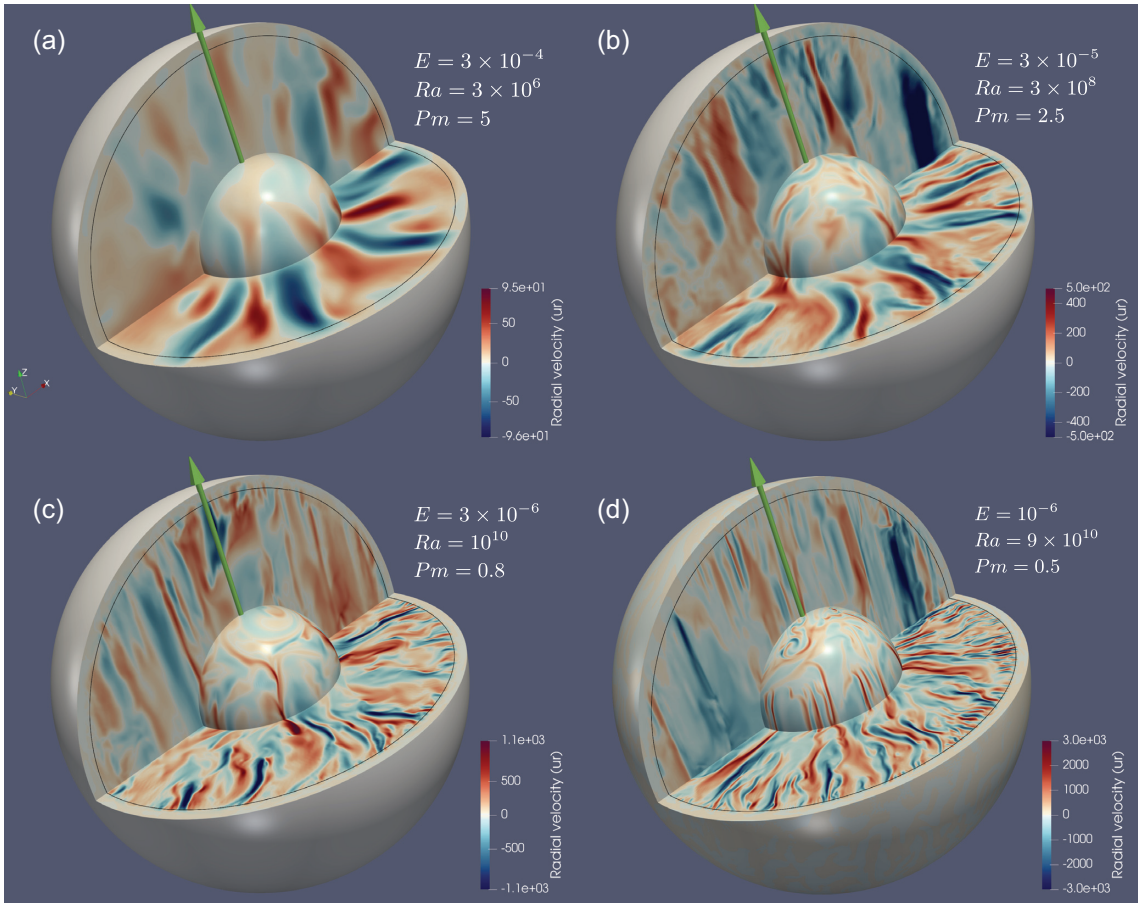

Figure 3. 3-D renderings of the radial velocity u_r for four dynamo models with the same stably stratified layer thickness ($r_s = 1.45$, $\mathcal{H}_s = 200$ km) and degree of stratification $N_m/\Omega \simeq 0.94$. For each panel, the solid lines delineates the radius of the stratified layer $r = r_s$, the green arrow highlights the rotation axis and the inner spherical surface corresponds to $r = 0.39\, r_o$.

Fig. 4(a) shows $\mathcal{L}_s$ and $\mathcal{L}_b$ as a function of the Ekman number for all the numerical models that feature a stably-stratified layer (i.e. $\Gamma > 0$). At the transition radius r_s, the convective flow lengthscale is found to follow a $\mathcal{L}_s \sim E^{1/3}$ law (solid line). This scaling reflects the local onset of convection beneath r_s where the available power content drops and yields weaker local convective supercriticality (see Fig. 1). The situation differs in the bulk of the convective core: while the flow lengthscale at $\mathcal{L}_b$ is almost identical to $\mathcal{L}_s$ when $E \geq 3 \times 10^{-5}$, the two lengthscales gradually depart from each other at lower Ekman numbers with $\mathcal{L}_b > \mathcal{L}_s$. This confirms the scale separation observed in the numerical simulations with the lowest Ekman numbers shown in the lower panels of Fig. 3.

The deviation from the viscous scaling $\mathcal{L}_b \sim E^{1/3}$ (e.g. King & Buffett 2013; Gastine *et al.* 2016) indicates that the underlying force balance which controls the convective flow is not dominated by viscous effects. Following Aubert *et al.* (2017) and Schwaiger *et al.* (2019), we analyse this force balance by decomposing each term that enter the Navier–Stokes equation (5) into spherical harmonics

$$F_{rms}^2 = \frac{1}{V} \int_{r_i+\lambda}^{r_o-\lambda} \sum_{\ell,m} F_{\ell m}^2 r^2 \mathrm{d}r = \sum_{\ell} F_{\ell}^2 \,, \tag{21}$$

where λ is the viscous boundary layer thickness. Fig. 4(b) illustrates the normalized force balance spectra in the fluid bulk for a selected numerical simulation with $E = 3 \times 10^{-6}$, $Ra = 10^{10}$, $r_s = 1.45$ (i.e. $\mathcal{H}_s = 200$ km) and $N_m/\Omega = 0.95$ using $\lambda = 10^{-2} d$. The leading order consists of a quasi-geostrophic (QG) force balance between Coriolis and pressure gradient. The ageostrophic Coriolis contribution which accounts for the difference between Coriolis and pressure forces, is then equilibrated by buoyancy at large scales and by Lorentz force at small scales. Inertia and viscosity lay one to two orders of magnitude below this second-order force balance. This force hierarchy forms the so-called *QG-MAC balance* introduced by Davidson (2013). This second-order force balance has been theoretically analysed in the plane layer geometry by Calkins (2018) using a multiscale expansion and was reported in direct numerical simulations in spherical geometry (e.g. Yadav *et al.* 2016; Schaeffer *et al.* 2017; Aubert *et al.* 2017). The force balance obtained in the numerical models with a 200-km-thick stably stratified layer atop the core is thus structurally akin to the force balance spectra of the fully convective simulations (e.g. Schwaiger *et al.* 2019).

3.2 Skin-effect and magnetic field smoothing

We now turn to examining the effect of the stable layer on the magnetic field structure. If one crudely assumes that the stable region is devoid of any fluid motion, it can be approximated by a layer of thickness $\mathcal{H}_s$ filled with an electrically conducting stagnant

Downloaded from https://academic.oup.com/gji/article-abstract/222/2/1433/5841194 by Biblio Planets user on 23 June 2020

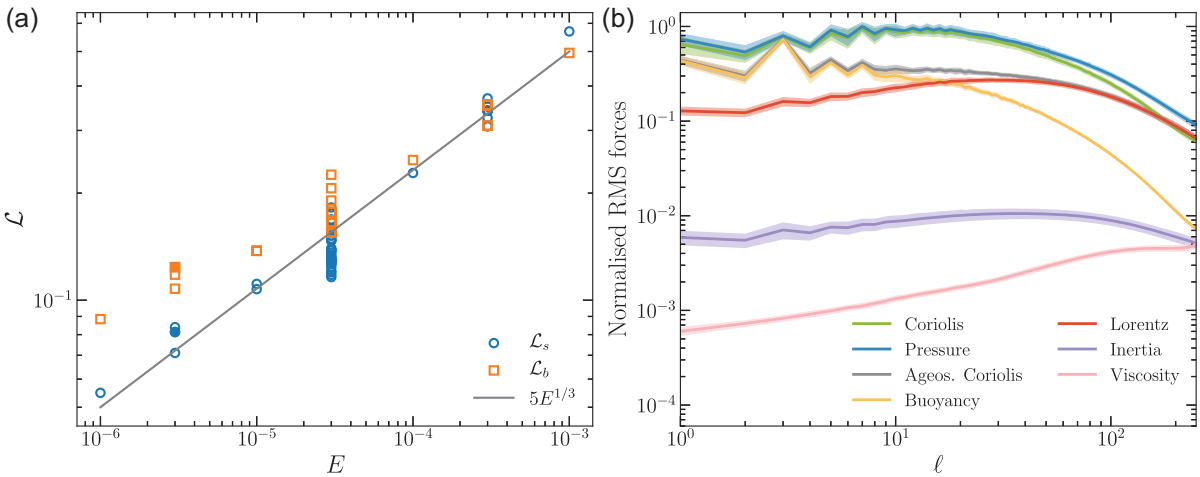

Figure 4. (a) Time-averaged convective flow lengthscale at r_s (i.e. $\mathcal{L}_s$) and at r_b (i.e. $\mathcal{L}_b$) as a function of the Ekman number E for all the numerical models with a stratified layer (i.e. $\Gamma > 0$). (b) Force balance spectra in the entire fluid bulk (eq. 21) normalized with respect to the maximum of the pressure force for a numerical simulation with $E = 3 \times 10^{-6}$, $Ra = 10^{10}$, $Pm = 0.8$, $r_s = 1.45$ (i.e. $\mathcal{H}_s = 200$ km) and $N_m/\Omega = 0.95$. The filled symbols in panel (a) correspond to the model described in panel (b).

fluid. This then acts as a *skin layer* that will attenuate the magnetic field amplitude by a factor $\exp(-\mathcal{H}_s/\delta)$, where δ is the magnetic skin depth defined by

$$\delta \sim \sqrt{\frac{\tau_\ell}{Pm}},$$

where curvature effects due to spherical geometry have been neglected. In the above expression, τ_ℓ corresponds to the typical turnover time $\tau_\ell \sim \mathcal{L}_s/Re$, where $Re = Rm/Pm$ is the fluid Reynolds number. This yields

$$\delta \sim (Rm\,\bar{\ell}_s)^{-1/2}. \tag{22}$$

The factor of attenuation of the magnetic energy due to the skin effect can hence be approximated by

$$\ln\left[\frac{\mathcal{M}_\ell(r_o)}{\mathcal{M}_\ell(r_s)}\right] \sim -\mathcal{H}_s(Rm\,\bar{\ell}_s)^{1/2}, \tag{23}$$

where $\mathcal{M}_\ell(r)$ corresponds to the magnetic energy at the spherical harmonic degree ℓ and at the radius r. From a practical stand-point, it is more convenient to assess the impact of a stable layer by a direct comparison of the magnetic energy at the CMB between a stably stratified case and its fully convective counterpart

$$\mathcal{Q}_\ell = \frac{\mathcal{M}_\ell^{\rm strat}(r_o)}{\mathcal{M}_\ell^{\rm FC}(r_o)}, \tag{24}$$

where the superscripts 'FC' and 'strat' stand for the fully convective and the stably stratified models, respectively. To relate the above expression to the skin effect (23), we make the two following hypotheses:

(i)We assume that the magnetic energy at the transition radius r_s is independent of the presence of a stable layer, that is $\mathcal{M}_\ell^{\rm strat}(r_s) \simeq \mathcal{M}_\ell^{\rm FC}(r_s)$,
(ii)We assume that the magnetic energy of the fully convective model at r_s is comparable to the energy at the CMB, that is $\mathcal{M}_\ell^{FC}(r_s) \simeq \mathcal{M}_\ell^{FC}(r_o)$.

The validity of those hypotheses will be further assessed below. Combining eq. (23) with the two previous assumptions yields the following scaling for the damping factor

$$\mathcal{Q}_\ell^{\rm SK} = \exp\left[-\alpha_{\rm SK}\mathcal{H}_s(Rm\,\bar{\ell}_s)^{1/2}\right], \tag{25}$$

where $\alpha_{\rm SK}$ is a proportionality coefficient that depends on the geometry. The above scaling should be understood as the maximum damping that a stable layer could yield in the idealized limit of vanishing fluid motions there, that is $\sup(\mathcal{Q}_\ell) = \mathcal{Q}_\ell^{\rm SK}$ when $N_m/\Omega \gg 1$.

Fig. 5 shows the time-averaged magnetic energy spectra at the CMB (panel a) and the damping factor $\mathcal{Q}_\ell$ (panel b) for one fully convective simulation and five numerical models with an increasing degree of stratification N_m/Ω (same models as in Fig. 1). The magnetic energy content decreases when increasing N_m/Ω. This energy drop is more pronounced for the smaller scales of the magnetic field. A saturation is observed for the models with $N_m/\Omega > 10$ for which the spectra become comparable. The damping factor $\mathcal{Q}_\ell$ drops accordingly when increasing N_m/Ω to tend towards the limit $\mathcal{Q}_\ell^{\rm SK}$, obtained here using the value of Rm of the fully convective simulation and $\alpha_{\rm SK} = 0.5$ (dashed line in Fig. 5b). This implies that for large degree of stratification $N_m/\Omega \gg 1$, a stable layer has a similar dynamic signature on the magnetic field as a passive conductor of the same thickness. This is not the case for intermediate stratification $N_m/\Omega \simeq 1$ for which convective motions can penetrate into the stable layer over some distance $\mathcal{D}_p$.

To further illustrate the magnetic field damping due to the presence of a stable layer, Fig. 6 shows snapshots of the radial component of the magnetic field at the radius r_s and at the CMB, for one fully convective model and three simulations with increasing N_m/Ω. At the transition radius r_s, the magnetic field structures of the four cases are relatively similar, featuring a dominant dipolar structure accompanied by intense localized flux concentration. The first hypothesis involved in the derivation of eq. (25) is hence roughly satisfied, though a small decay of magnetic field amplitude with N_m/Ω is visible. This can be likely attributed to the decreasing available buoyancy power in the upper regions of the convective part (see Fig. 1a). For the fully convective simulation, the magnetic field structure remains very similar at the CMB, validating the second assumption used when deriving eq. (25). In contrast, the stably stratified layer reduces the magnetic field amplitude and acts as a low-pass filter on the magnetic field structures gradually filtering out the small-scale features when N_m/Ω increases. While inverse polarity patches are for instance still discernible on the $N_m/\Omega = 1.64$ case (Fig. 6b), they disappear completely in the most stratified

Downloaded from https://academic.oup.com/gji/article-abstract/222/2/1433/5841194 by Biblio Planets user on 23 June 2020

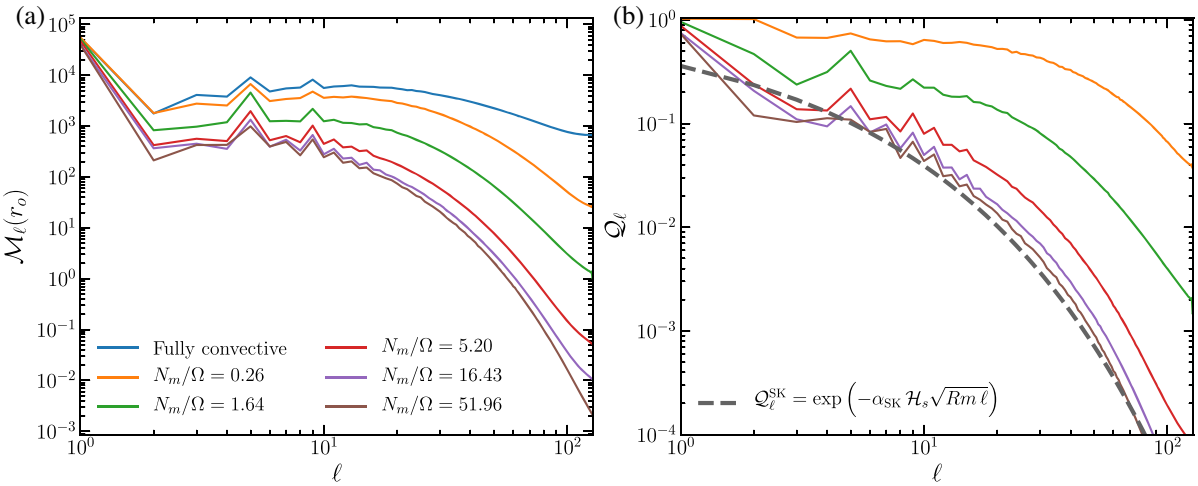

Figure 5. (a) Time-averaged magnetic energy at the CMB $\mathcal{M}_\ell(r_o)$ as a function of the spherical harmonic degree ℓ for numerical models with $E = 3 \times 10^{-5}$, $Ra = 3 \times 10^8$, $Pm = 2.5$, $r_s = 1.45$ (i.e. $\mathcal{H}_s = 200$ km) and increasing values of N_m/Ω (same models as in Fig. 1). (b) Damping of the magnetic energy at the CMB relative to the fully convective case $\mathcal{Q}_\ell$ (eq. 24) as a function of ℓ. The dashed grey line corresponds to the scaling Eq. (25) using $\alpha_{\rm SK} = 0.5$ and the time-averaged magnetic Reynolds number of the fully convective case, that is $Rm = 536$.

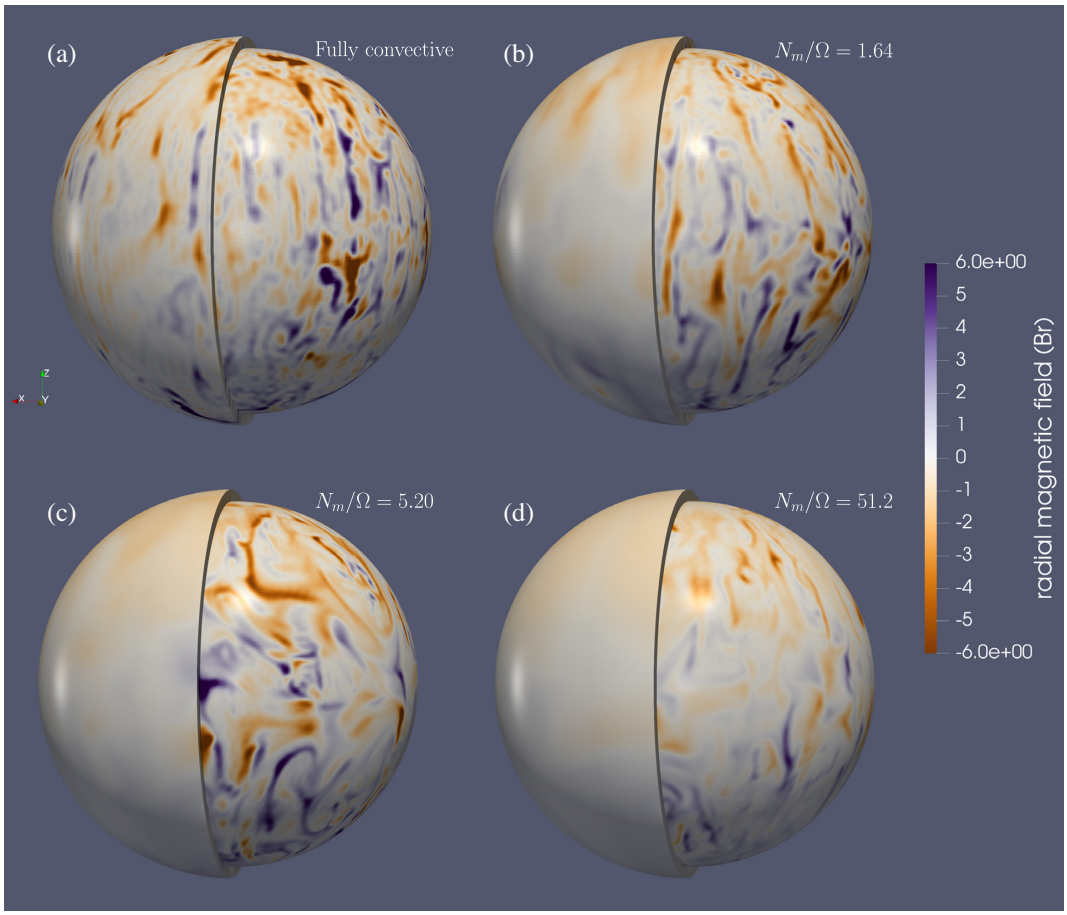

Figure 6. 3-D renderings of the radial component of the magnetic field B_r for four numerical models with the same control parameters $E = 3 \times 10^{-5}$, $Ra = 3 \times 10^8$, $Pm = 2.5$ and increasing degree of stratification N_m/Ω. The stratified cases have $r_s = 1.45$ (i.e. $\mathcal{H}_s = 200$ km). The inner spheres correspond to $r = r_s$ and the outer ones to the CMB. The magnetic field amplitude is expressed in units of the square root of the Elsasser number.

case with $N_m/\Omega = 51.2$ (Fig. 6d). We can hence anticipate that large degree of stratification will yield smooth CMB magnetic fields incompatible with the observed geomagnetic field (see Christensen 2018).

3.3 Earth-likeness

For a more quantitative assessment, we now compare the morphology of the magnetic fields produced in the numerical models to the

Downloaded from https://academic.oup.com/gji/article-abstract/222/2/1433/5841194 by Biblio Planets user on 23 June 2020

geomagnetic field at the CMB in terms of the four criteria introduced by Christensen *et al.* (2010). As shown in Fig. 6, the impact of the stable layer on the magnetic field morphology directly depends on the ratio N_m/Ω and hence on the distance of penetration $\mathcal{D}_p$ (Fig. 2). We now define a dynamic *effective thickness* $\mathcal{H}_{\rm eff}$ of the stable layer, which removes the distance of penetration of the convective eddies $\mathcal{D}_p$ from the actual static thickness $\mathcal{H}_s$, such that

$$\mathcal{H}_{\rm eff} = \mathcal{H}_s - \mathcal{D}_p = r_o - r_p \,. \tag{26}$$

We introduce this quantity to better capture the effective lengthscale that controls the magnetic field smoothing via the skin effect. Fig. 7 shows the time-averages and the standard deviations of the four rating parameters AD/NAD, O/E, Z/NZ and FCF (Christensen *et al.* 2010) as a function of $\mathcal{H}_{\rm eff}$. The series of numerical models with $E = 3 \times 10^{-4}$ and $Ra = 3 \times 10^6$ have been excluded from this plot since the fully convective simulation features a weakly dipolar magnetic field and $\chi^2 > 8$. The relative axial dipole power AD/NAD (Fig. 7a) is the criterion that shows the strongest dependence to the presence of a stable layer. The vast majority of the models with a thin or a vanishing stable layer (i.e. $\mathcal{H}_{\rm eff} \simeq 0$ km) indeed show AD/NAD values that lie within the 1σ tolerance level of the nominal Earth's value. In contrast, the numerical models with $\mathcal{H}_{\rm eff} > 10$ km yield too dipolar magnetic field with AD/NAD ratios that grow well above the favoured value. In addition to the increase of AD/NAD, the stable stratification also makes the CMB magnetic field more antisymmetric with respect to the equator (Fig. 7b) and more axisymmetric (Fig. 7c), yielding O/E and Z/NZ ratios larger than the expected Earth's value. The flux concentration FCF shows a slightly different behaviour since weakly stratified or fully convective models sometimes present ratios slightly larger than the nominal value, though they mostly lie within the 1σ tolerance range.

Overall the observed tendency is very similar for the four rating parameters: an increase of $\mathcal{H}_{\rm eff}$ goes along with a gradual smoothing of the CMB magnetic field which becomes more and more dipolar and axisymmetric. This analysis also demonstrates that $\mathcal{H}_{\rm eff}$ is the key physical parameter that governs the Earth-likeness of the magnetic field independently of the variations of E, Pm and Ra. The optimal numerical models which show the best agreement with the Earth CMB field in terms of χ^2 values correspond to a vanishing effective thickness of the stable layer. This implies that to get a reasonable agreement with the geomagnetic field, the numerical models require either no stratified layer, or a penetration distance which is sufficient to span the entire static thickness of the layer. This yields the following upper bound for the thickness of the stable layer

$$\mathcal{H}_s \leq \mathcal{D}_p \,. \tag{27}$$

Using the scaling for the penetration distance (19), one gets

$$\mathcal{H}_s \leq 3.2 \left(\frac{\mathcal{N}}{\Omega} \bar{\ell}_s \right)^{-1} , \tag{28}$$

in dimensionless units. The above scaling relation could be further simplified by replacing $\bar{\ell}_s$ by the onset scaling obtained in Fig. 4(a). Given the uncertainties when extrapolating numerical geodynamo models to Earth core conditions, we rather keep $\bar{\ell}_s$ for further discussion of the geophysical implications of eq. (28).

To further test the validity of this upper bound, we focus on the 36 numerical simulations with $E = 3 \times 10^{-5}$ and $Ra = 3 \times 10^8$ for which the parameter space ($\mathcal{H}_s$, N_m/Ω) has been more densely sampled. Fig. 8 shows the morphological semblance χ^2 in the ($\mathcal{H}_s$, N_m/Ω) parameter space for this subset of simulations at fixed Ekman and Rayleigh numbers. For a practical determination of the upper bound given in eq. (28) and shown as a dashed line in Fig. 8, we use $\bar{\ell}_s = 35$ (see Table A1) and make the assumption that $\mathcal{N} \simeq N_m$. The analysis of the distance of penetration (Fig. 2a) has already shown that this is a rather bold hypothesis that in practice yields some dispersion of the data around the theoretical scaling (2). This approximation is however mandatory for a comparison of the numerical models with the geophysical estimates. Indeed, while several studies suggest possible values of the maximum of the Brunt–Väisälä frequency N_m for the Earth core (see Table 1), $\mathcal{N}$ cannot be determined without the knowledge of $\mathcal{D}_p$, making its geophysical estimate rather uncertain. Despite this approximation, the scaling relation (28) is found to correctly capture the transition between the numerical models with a good morphological agreement with the geomagnetic field (blue symbols with $\chi^2 < 4$) from those which are non-compliant due their too dipolar structure.

4 GEOPHYSICAL IMPLICATIONS

The condition (27) puts a strong geophysical constraint on the acceptable degree of stratification. For a comparison with the geophysical estimates of the physical properties of a stable layer at the top of the core coming from both seismic and magnetic studies, we report in Fig. 8 the values of $\mathcal{H}_s$ and N_m/Ω coming from the studies listed in Table 1. Due to the magnetic field smoothing by skin effect, we fail to produce any Earth-like dynamo model with a stratification degree of $N_m/\Omega \geq 10$ even for thicknesses as low as $\mathcal{H}_s = 50$ km. Hence, a stable layer with $\mathcal{H}_s \geq 100$ km and a stratification degree of $N_m/\Omega \simeq 10$ suggested by some seismic studies (Helffrich & Kaneshima 2010; Tang *et al.* 2015; Kaneshima 2018) or of $N_m/\Omega > 20$ in models with a stable layer of compositional origin (Buffett & Seagle 2010; Gubbins & Davies 2013) seem hard to reconcile with our numerical geodynamo models. The condition (27) can also be confronted to the estimates of outer core stratification that come from physical interpretation of the geomagnetic secular variation (Braginsky 1993; Buffett *et al.* 2016). In agreement with the previous findings by Olson *et al.* (2017), Yan & Stanley (2018) and Christensen (2018), the numerical simulations with $E = 3 \times 10^{-5}$ yield an Earth-like magnetic field morphology when $\mathcal{H}_s \sim 100$ km and $N_m \sim \Omega$. However, since the penetration distance directly depends on the horizontal lengthscale of the convective flow, the threshold obtained in Fig. 8 using numerical simulations with $E = 3 \times 10^{-5}$ shall become more stringent at lower Ekman numbers when the convective flow lengthscale at r_s is smaller.

To document this property, Fig. 9 shows the evolution of χ^2 for three sets of numerical simulations with $N_m/\Omega \in [0, 0.47, 0.95]$ and $\mathcal{H}_s \in [0, 155, 200]$ km for Ekman numbers decreasing from $E = 3 \times 10^{-5}$ to $E = 10^{-6}$. The numerical models which are fully convecting remain in excellent morphological agreement with the geomagnetic field (i.e. $\chi^2 < 2$) for the three Ekman numbers considered here. A closer inspection of the four rating parameters however reveals a slow tendency to get more and more dipole-dominated magnetic fields when E decreases. This increasing AD/NAD ratio is compensated by the evolution of FCF which is getting closer to the expected Earth value at lower E. The numerical models with a stably stratified layer with a weak stratification $N_m/\Omega = 0.47$ or $N_m/\Omega = 0.95$ show a stronger dependence to the Ekman number: while the $E = 3 \times 10^{-5}$ cases still feature Earth-like magnetic

Downloaded from https://academic.oup.com/gji/article-abstract/222/2/1433/5841194 by Biblio Planets user on 23 June 2020

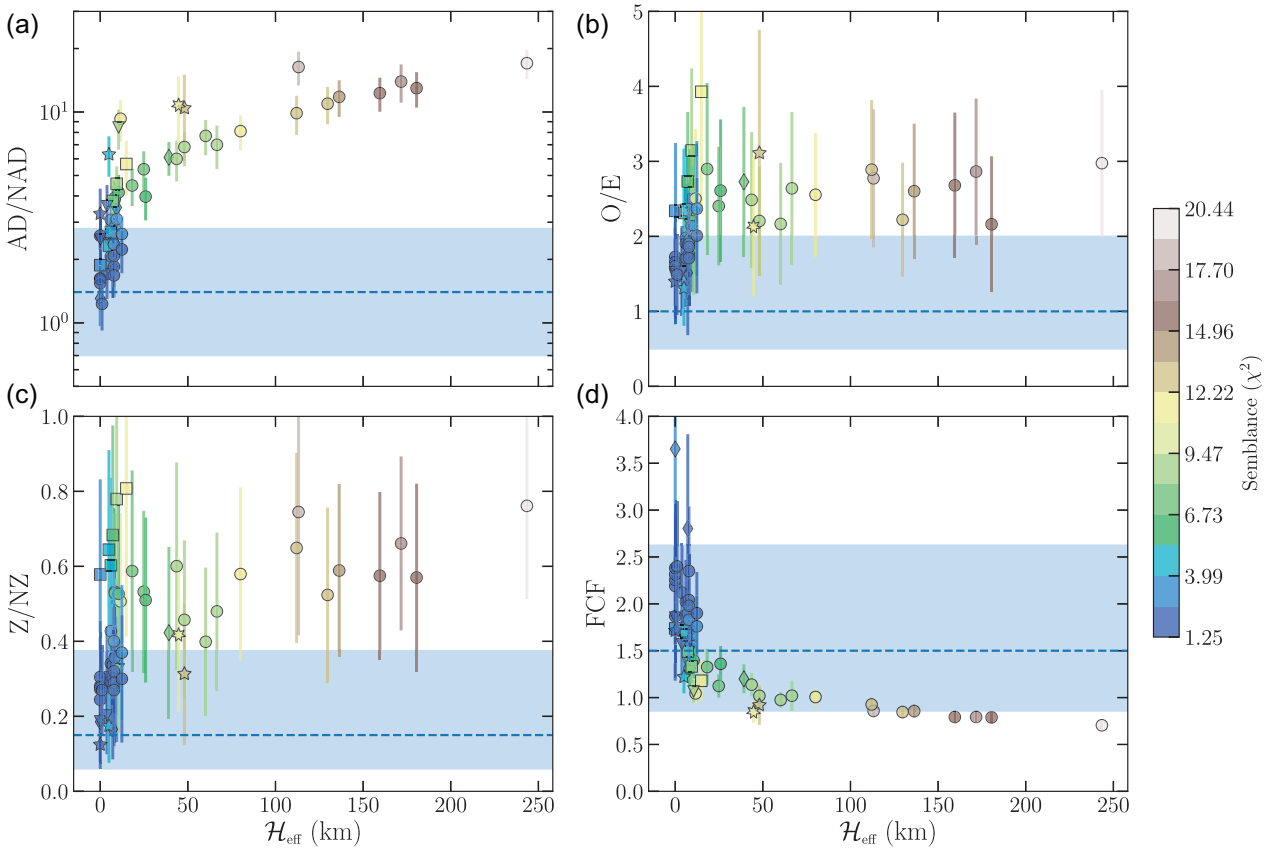

Figure 7. (a) AD/NAD as a function of the effective thickness of the stably stratified layer $\mathcal{H}_{\rm eff} = r_o - r_p$. (b) O/E as a function of $\mathcal{H}_{\rm eff}$. (c) Z/NZ as a function of $\mathcal{H}_{\rm eff}$. (d) FCF as a function of $\mathcal{H}_{\rm eff}$. The colour of the symbols scale with the value of the semblance χ^2, while the shape of the symbols change with the combination of parameters (E, Ra) following the symbols already used in Fig. 2. The errorbars correspond to one standard deviation about the mean values. The dashed horizontal lines show the nominal values for the geomagnetic field, while the blue shaded area correspond to one standard deviation in logarithmic scale (Christensen *et al.* 2010). Given their poor Earth-likeness, the simulations with $E \geq 3 \times 10^{-4}$ have been excluded from these plots.

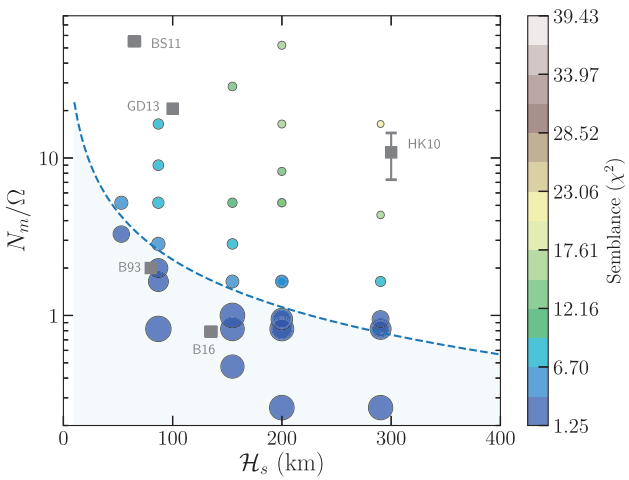

Figure 8. Morphological semblance between the numerical magnetic fields and the geomagnetic field at the CMB quantified by the measure of χ^2 in the ($\mathcal{H}_s$, N_m/Ω) parameter space for all the numerical simulations with fixed Ekman and Rayleigh numbers ($E = 3 \times 10^{-5}$ and $Ra = 3 \times 10^8$). The size of the symbols is inversely proportional to the value of χ^2. The dashed blue line corresponds to the bound (28) derived using $\bar{\ell}_s = 35$ (see Table A1) and assuming that $\mathcal{N} \simeq N_m$. The blue shaded region corresponds to the condition (27). The different studies listed in Table 1 are marked by grey squares.

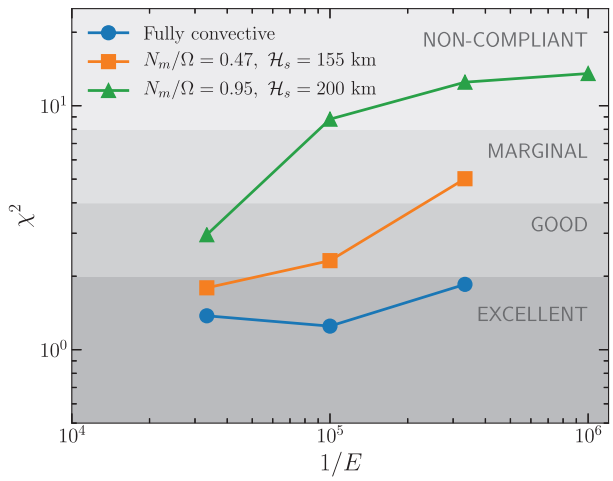

Figure 9. Compliance of field morphology quantified by its χ^2 as a function of the Ekman number E for three fully convective models (circles), three numerical models with $N_m/\Omega = 0.47$ and $\mathcal{H}_s = 155$ km (squares) and four numerical models with $N_m/\Omega = 0.95$ and $\mathcal{H}_s = 200$ km (triangle)s. The grey shaded regions mark the boundaries of different levels of agreement with the Earth's magnetic field introduced by Christensen *et al.* (2010).

Downloaded from https://academic.oup.com/gji/article-abstract/222/2/1433/5841194 by Biblio Planets user on 23 June 2020

fields, the compliance χ^2 quickly degrades at lower E, yielding too dipolar and too axisymmetric magnetic fields incompatible with the geomagnetic observations. This is directly related to the decrease of the convective flow lengthscale which is found to follow $\bar{\ell}_s \sim E^{-1/3}$ atop the convective core (Fig. 4a). This goes along with smaller penetration distance $\mathcal{D}_p$ and hence larger $\mathcal{H}_{\rm eff}$ which then yield an increased filtering of the CMB field by skin effect. For the lowest Ekman number considered here, we hence fail to produce an Earth-like magnetic field at a parameter combination $(\mathcal{H}_s, N_m/\Omega)$ very close to the best-fitting models by Buffett *et al.* (2016).

Dynamo models carry their own limitations and we can hence wonder whether there would be some leeway to viable (from a geomagnetic standpoint) stratification at Earth's core conditions. Here we envision three different scenarios to alleviate the severe limitation (28):

Larger distance of penetration: A way to maintain $\mathcal{H}_{\rm eff} = 0$ km at a given value of $\mathcal{H}_s$ would require an increase of the penetration distance. Based on the penetration distance of Alfvén waves, Takehiro (2015) for instance suggests that the hydrodynamic scaling (2) should be replaced by

$$\mathcal{D}_p \sim \frac{Lu}{\bar{\ell}_s^2}, \quad Lu = \frac{2}{1+Pm}\left(\frac{\Lambda\, Pm}{E}\right)^{1/2},$$

when magnetic effects become important, Lu being the Lundquist number (e.g. Schaeffer *et al.* 2012). At Earth's core conditions, this might yield much larger penetration distances than (2) (see Takehiro & Sasaki 2018a). Though a transition to the above scaling at a parameter range not covered in this study cannot be ruled out, our simulations do not show any correlation between the penetration distance $\mathcal{D}_p$ and the ratio $Lu/\bar{\ell}_s^2$. Furthermore, Takehiro (2015) specifically studied Alfvén wave penetration, which is rather different from the problem of penetrating convection in dynamo models. In the latter, the hydromagnetic waves indeed exist at a significantly smaller level than the background magnetic field which is rather shaped by the slow convective motions (e.g. Hori *et al.* 2015; Aubert 2018). In this context, we do not anticipate that Alvén wave dynamics can have a significant impact on the attenuation properties of the background magnetic field.

Larger convective flow lengthscale at r_s: The penetration distance directly depends on the horizontal lengthscale of the convective flow at the base of the stable layer $\mathcal{L}_s$. Given that the local convective supercriticality drops atop the convective core, the flow lengthscale at r_s follows a local onset scaling of the form $\mathcal{L}_s \sim E^{1/3}$, or equivalently $\bar{\ell}_s \sim E^{-1/3}$. At Earth's core conditions with $E = 10^{-15}$ and $N_m \sim \Omega$, the penetration distance would be of the order 100 m, would this onset scaling still hold. Given the large diffusivities of the 3-D calculations, a transition to a magnetic control of $\bar{\ell}_s$ cannot be ruled out. The theoretical prediction by Davidson (2013) for a QG-MAC balance would then yield $\bar{\ell}_s \sim Ro^{-1/4}$ and hence $\mathcal{D}_p \sim 400$ km when using $Ro = ReE \sim 10^{-5}$ and $N_m \sim \Omega$. However, while there is supporting evidence that the convective lengthscale in the bulk of the convective core departs from viscous control (see Fig. 4a and Aubert *et al.* 2017; Schwaiger *et al.* 2019), our simulations do not suggest that the interface flow at r_s should follow the same scaling.

Additional physical forcings in the stable layer: The last avenue to alleviate the criterion (28) relies on additional forcings to drive flows in the stably stratified layer. In contrast to the assumptions made in this study, the CMB heat flow is expected to be strongly heterogeneous and hence drive flows by thermal winds. Using dynamo models with a stable layer with $N_m/\Omega \leq 4$ and an heterogeneous heat flux pattern, Christensen (2018) has derived a scaling relation for the flow driven by the CMB thermal heterogeneities. At Earth's core conditions, this flow is expected to be very shallow limited to the first few hundred meters below the CMB and might hence have a moderate impact on the magnetic field morphology, would the extrapolation from geodynamo simulations to Earth condition holds. Because of the strong core–mantle heat flux heterogeneities, the stratification might not be global but rather confined to localized regions as suggested by the hydrodynamic numerical simulations by Mound *et al.* (2019). Regional stratification could however yield a heterogeneous magnetic field at the CMB with a weaker field with a smoother morphology in the stratified area. The viability of this scenario remains hence to be assessed by means of global geodynamo models. Other physical forcings not accounted for in our models, such as double-diffusive effects, could possibly impact the dynamics of the outer layer. A promising physical configuration arises when thermal stratification is stable while compositional stratification is unstable, a configuration akin to fingering convection that develops in the ocean when warm and salty water lies above cold and fresh water (e.g. Radko 2013). Numerical models by Manglik *et al.* (2010) and Takahashi *et al.* (2019), carried out in the context of modelling Mercury's dynamo, indicate that fingering convection enhances the convective penetration in the thermally stratified layer when $N_m \sim \Omega$ (see also Monville *et al.* 2019; Silva *et al.* 2019; Bouffard *et al.* 2019).

5 CONCLUSION

In this study, we have examined the physical effect of a stably stratified layer underneath the CMB by means of 3-D global geodynamo simulations in spherical geometry. We have introduced a parametrized temperature background to independently vary the thickness $\mathcal{H}_s$ and the degree of stratification of the stable layer, quantified here by the ratio of the maximum Brunt–Väisälä frequency over the rotation rate N_m/Ω. We have conducted a systematic survey by varying $\mathcal{H}_s$ from 0 to 290 km and N_m/Ω from 0 to more than 50 for several combinations of Ekman and Rayleigh numbers. This parameter range encompasses the possible values of the physical properties of a stable layer underneath the CMB that come either from seismic or from geomagnetic studies (see Table 1). This work complements previous analyses that were either limited to moderate stratification degree $N_m/\Omega < 5$ (Olson *et al.* 2017; Yan & Stanley 2018; Christensen 2018) or to moderate control parameters like large Ekman numbers ($E = 3 \times 10^{-4}$, Nakagawa 2011) or dynamo action close to onset (Nakagawa 2015).

We have first studied the penetration of the convective motions in the stably stratified layer. When using the radial profile of the buoyancy power to define the penetration distance $\mathcal{D}_p$, we have shown that $\mathcal{D}_p \sim (\mathcal{N}\bar{\ell}_s/\Omega)^{-1}$ where $\mathcal{N}$ incorporates the local variation of the Brunt–Väisälä frequency and $\bar{\ell}_s$ relates to the typical size of the convective eddies $\mathcal{L}_s$ at the top of the convective core via $\bar{\ell}_s = \pi r_s/\mathcal{L}_s$. This scaling is in perfect agreement with the theoretical prediction by Takehiro & Lister (2001) which has been derived in absence of magnetic effects. Because of the drop of the convective supercriticality at the top of the convective core, the convective lengthscale at the transition radius r_s has been found to follow an onset scaling, that is $\mathcal{L}_s \sim E^{1/3}$. Our results hence indicate that the magnetic field has little influence on the penetration distance, in contrast with the theoretical expectations by Takehiro (2015). To explain this somewhat surprising result, we note that when the

Downloaded from https://academic.oup.com/gji/article-abstract/222/2/1433/5841194 by Biblio Planets user on 23 June 2020

magnetic field is self-sustained -as opposed to the imposed field considered by Takehiro & Sasaki (2018a)-, hydromagnetic waves have a much weaker amplitude than the background magnetic field which is rather shaped by the slow convective motions (e.g. Hori *et al.* 2015). We hence anticipate that the dynamics of the Alvén waves at r_s have little impact on the distance of penetration of the convective features.

Stable stratification has a strong impact on the magnetic field morphology at the CMB. Because of vanishing convective flows in the stable layer, the small-scale features of the magnetic field are smoothed out by skin effect (e.g. Christensen 2006; Gubbins 2007). Using the rating parameters defined by Christensen *et al.* (2010) to assess the Earth likeness of the numerical models fields, we have shown that the physically relevant lengthscale is the *effective thickness* of the stable layer $\mathcal{H}_{\rm eff}$, which results from the difference between the actual static thickness $\mathcal{H}_s$ and the penetration distance $\mathcal{D}_p$. Only models with a vanishing $\mathcal{H}_{\rm eff}$ yield a good agreement with the Earth CMB field. This implies that Earth-like dynamo models either harbour a fully convecting core or have a penetration distance which is sufficient to cross the entire stable layer. The combination of the scaling obtained for the penetration distance $\mathcal{D}_p$ and the condition $\mathcal{H}_{\rm eff} = 0$ km yields the following upper bound for the thickness of the stable layer underneath the CMB

$$\mathcal{H}_s \leq \left(\frac{N_m}{\Omega}\right)^{-1} \mathcal{L}_s \, .$$

This condition puts severe limitations on the acceptable degree of stratification. Large degrees of $N_m/\Omega \sim 10$ suggested by several seismic studies (e.g. Helffrich & Kaneshima 2010) yield magnetic field morphology that are incompatible with the geomagnetic field observations at the CMB even for a layer as small as $\mathcal{H}_s = 50$ km. In agreement with previous findings by Olson *et al.* (2017) and Christensen (2018), we have shown that geodynamo models with a smaller stratification $N_m \sim \Omega$ and $\mathcal{H}_s \sim 100$ km sustain a magnetic field morphology that is compatible with the geomagnetic observations, as long as the Ekman number is large enough, that is $E \geq 3 \times 10^{-5}$. Since the convective lengthscale at the top of the convective core decreases with the Ekman number, following the onset scaling $\mathcal{L}_s \sim E^{1/3}$, the penetration distance decreases and the Earth-likeness of the numerical models fields degrades. At Earth's core conditions with $E = 10^{-15}$ and $N_m \sim \Omega$, the penetration distance could be reduced to hundreds of metre, yielding a strong magnetic skin effect incompatible with geomagnetic observations.

Consequently, our suite of numerical models, given the type and magnitude of physical processes governing the dynamics of the stably stratified layer that they incorporate, favour the absence of stable stratification atop Earth's core.

ACKNOWLEDGEMENTS

We would like to thank Maylis Landeau and Vincent Lesur for fruitful discussions during the elaboration of this manuscript. We acknowledge support from the Fondation Simone et Cino Del Duca of Institut de France (JA, 2017 Research Grant) and from CNRS Programme National de Planétologie (TG, 2017 PNP Grant). Numerical computations have been carried out on the S-CAPAD platform at IPGP and using HPC resources from GENCI (Grants A0040402122, A0070410095 and 2019gch0411). All the figures have been generated using `matplotlib` (Hunter 2007) and `paraview` (https://www.paraview.org).

REFERENCES

Alexandrakis, C. & Eaton, D.W., 2010. Precise seismic-wave velocity atop Earth's core: no evidence for outer-core stratification, *Phys. Earth planet. Inter.,* **180**(1–2), 59–65.

Amit, H., 2014. Can downwelling at the top of the Earth's core be detected in the geomagnetic secular variation?, *Phys. Earth planet. Inter.,* **229,** 110–121.

Aubert, J., 2018. Geomagnetic acceleration and rapid hydromagnetic wave dynamics in advanced numerical simulations of the geodynamo, *Geophys. J. Int.,* **214**(1), 531–547.

Aubert, J., Aurnou, J. & Wicht, J., 2008. The magnetic structure of convection-driven numerical dynamos, *Geophys. J. Int.,* **172**(3), 945–956.

Aubert, J., Gastine, T. & Fournier, A., 2017. Spherical convective dynamos in the rapidly rotating asymptotic regime, *J. Fluid Mech.,* **813,** 558–593.

Baerenzung, J., Holschneider, M. & Lesur, V., 2016. The flow at the Earth's core-mantle boundary under weak prior constraints, *J. geophys. Res.,* **121**(3), 1343–1364.

Bouffard, M., Choblet, G., Labrosse, S. & Wicht, J., 2019. Chemical convection and stratification in the Earth's outer core, *Front. Earth Sci.,* **7,** 99.

Boyd, J.P., 2001. *Chebyshev and Fourier Spectral Methods, Dover Books on Mathematics,* 2nd revised edn, Dover Publications, ISBN 0486411834.

Braginsky, S.I., 1993. MAC-oscillations of the hidden ocean of the core, *J. Geomag. Geoelectr.,* **45,** 1517–1538.

Brodholt, J. & Badro, J., 2017. Composition of the low seismic velocity E' layer at the top of Earth's core, *Geophys. Res. Lett.,* **44**(16), 8303–8310.

Brown, B.P., Vasil, G.M. & Zweibel, E.G., 2012. Energy conservation and gravity waves in sound-proof treatments of stellar interiors. Part I. Anelastic approximations, *Astrophys. J.,* **756**(2), 109.

Browning, M., Brun, A.S. & Toomre, J., 2004. Simulations of core convection in rotating A-type stars: differential rotation and overshooting, *ApJ,* **601**(1), 512–529.

Brun, A.S., Miesch, M.S. & Toomre, J., 2011. Modeling the dynamical coupling of solar convection with the radiative interior, *Astrophys. J.,* **742**(2), 79.

Brun, A.S. *et al.*, 2017. On differential rotation and overshooting in solar-like stars, *Astrophys. J.,* **836**(2), 192.

Buffett, B., 2014. Geomagnetic fluctuations reveal stable stratification at the top of the Earth's core, *Nature,* **507,** 484–487.

Buffett, B., Knezek, N. & Holme, R., 2016. Evidence for MAC waves at the top of Earth's core and implications for variations in length of day, *Geophys. J. Int.,* **204,** 1789–1800.

Buffett, B.A. & Seagle, C.T., 2010. Stratification of the top of the core due to chemical interactions with the mantle, *J. geophys. Res.,* **115,** B04407.

Calkins, M.A., 2018. Quasi-geostrophic dynamo theory, *Phys. Earth planet. Inter.,* **276,** 182–189.

Christensen, U., 2018. Geodynamo models with a stable layer and heterogeneous heat flow at the top of the core, *Geophys. J. Int.,* **215,** 1338–1351.

Christensen, U., Olson, P. & Glatzmaier, G.A., 1999. Numerical modelling of the geodynamo: a systematic parameter study, *Geophys. J. Int.,* **138**(2), 393–409.

Christensen, U.R., 2006. A deep dynamo generating Mercury's magnetic field, *Nature,* **444,** 1056–1058.

Christensen, U.R. & Aubert, J., 2006. Scaling properties of convection-driven dynamos in rotating spherical shells and application to planetary magnetic fields, *Geophys. J. Int.,* **166,** 97–114.

Christensen, U.R. & Wicht, J., 2008. Models of magnetic field generation in partly stable planetary cores: applications to Mercury and Saturn, *Icarus,* **196,** 16–34.

Christensen, U.R. & Wicht, J., 2015. 8.10 - Numerical dynamo simulations, in *Treatise on Geophysics,* 2nd edn, pp. 245–277, ed. Schubert, G., Elsevier.

Downloaded from https://academic.oup.com/gji/article-abstract/222/2/1433/5841194 by Biblio Planets user on 23 June 2020

Christensen, U.R., Aubert, J. & Hulot, G., 2010. Conditions for Earth-like geodynamo models, *Earth planet. Sci. Lett.,* **296,** 487–496.

Davidson, P.A., 2013. Scaling laws for planetary dynamos, *Geophys. J. Int.,* **195**(1), 67–74.

de Koker, N., Steinle-Neumann, G. & Vlček, V., 2012. Electrical resistivity and thermal conductivity of liquid Fe alloys at high P and T, and heat flux in Earth's core, *Proc. Natl. Acad. Sci.,* **109,** 4070–4073.

Deng, L. & Xiong, D.R., 2008. How to define the boundaries of a convective zone, and how extended is overshooting?, *MNRAS,* **386**(4), 1979–1989.

Dietrich, W. & Wicht, J., 2018. Penetrative convection in partly stratified rapidly rotating spherical shells, *Front. Earth Sci.,* **6,** 189.

Dormy, E., Cardin, P. & Jault, D., 1998. MHD flow in a slightly differentially rotating spherical shell, with conducting inner core, in a dipolar magnetic field, *Earth planet. Sci. Lett.,* **160**(1-2), 15–30.

Gastine, T., Wicht, J. & Aubert, J., 2016. Scaling regimes in spherical shell rotating convection, *J. Fluid Mech.,* **808,** 690–732.

Glatzmaier, G.A., 1984. Numerical simulations of stellar convective dynamos. I. The model and method, *J. Comput. Phys.,* **55,** 461–484.

Gomi, H., Ohta, K., Hirose, K., Labrosse, S., Caracas, R., Verstraete, M.J. & Hernlund, J.W., 2013. The high conductivity of iron and thermal evolution of the Earth's core, *Phys. Earth planet. Inter.,* **224,** 88–103.

Gubbins, D., 2007. Geomagnetic constraints on stratification at the top of Earth's core, *Earth, Planets, Space,* **59,** 661–664.

Gubbins, D. & Davies, C.J., 2013. The stratified layer at the core-mantle boundary caused by barodiffusion of oxygen, sulphur and silicon, *Phys. Earth planet. Inter.,* **215,** 21–28.

Helffrich, G. & Kaneshima, S., 2010. Outer-core compositional stratification from observed core wave speed profiles, *Nature,* **468,** 807–810.

Helffrich, G. & Kaneshima, S., 2013. Causes and consequences of outer core stratification, *Phys. Earth planet. Inter.,* **223,** 2–7.

Hirose, K., Labrosse, S. & Hernlund, J., 2013. Composition and state of the core, *Ann. Rev. Earth Planet. Sci.,* **41,** 657–691.

Hori, K., Jones, C.A. & Teed, R.J., 2015. Slow magnetic Rossby waves in the Earth's core, *Geophys. Res. Lett.,* **42**(16), 6622–6629.

Hunter, J.D., 2007. Matplotlib: a 2D graphics environment, *Compu. Sci. Eng.,* **9**(3), 90–95.

Hurlburt, N.E., Toomre, J., Massaguer, J.M. & Zahn, J.-P., 1994. Penetration below a convective zone, *Astrophys. J.,* **421,** 245–260.

Irving, J.C.E., Cottaar, S. & Lekić, V., 2018. Seismically determined elastic parameters for Earth's outer core, *Sci. Adv.,* **4**(6), doi:10.1126/sciadv.aar2538.

Jault, D. & Le Mouël, J.L., 1991. Physical properties at the top of the core and core surface motions, *Phys. Earth planet. Inter.,* **68**(1-2), 76–84.

Kaneshima, S., 2018. Array analyses of SmKS waves and the stratification of Earth's outermost core, *Phys. Earth planet. Inter.,* **276,** 234–246.

Kaneshima, S. & Matsuzawa, T., 2015. Stratification of earth's outermost core inferred from SmKS array data, *Prog. Earth Planet. Sci.,* **2,** 15.

King, E.M. & Buffett, B.A., 2013. Flow speeds and length scales in geodynamo models: the role of viscosity, *Earth planet. Sci. Lett.,* **371,** 156–162.

Konôpková, Z., McWilliams, R.S., Gómez-Pérez, N. & Goncharov, A.F., 2016. Direct measurement of thermal conductivity in solid iron at planetary core conditions, *Nature,* **534**(7605), 99–101.

Kosloff, D. & Tal-Ezer, H., 1993. A modified Chebyshev pseudospectral method with an O(N^{-1}) time step restriction, *J. Comput. Phys.,* **104**(2), 457–469.

Lay, T. & Young, C.J., 1990. The stably-stratified outermost core revisited, *Geophys. Res. Lett.,* **17**(11), 2001–2004.

Lay, T., Hernlund, J. & Buffett, B.A., 2008. Core-mantle boundary heat flow, *Nat. Geosci.,* **1,** 25–32.

Lesur, V., Whaler, K. & Wardinski, I., 2015. Are geomagnetic data consistent with stably stratified flow at the core-mantle boundary?, *Geophys. J. Int.,* **201**(2), 929–946.

Lister, J.R. & Buffett, B.A., 1995. The strength and efficiency of thermal and compositional convection in the geodynamo, *Phys. Earth planet. Inter.,* **91,** 17–30.

Lister, J.R. & Buffett, B.A., 1998. Stratification of the outer core at the core-mantle boundary, *Phys. Earth planet. Inter.,* **105**(1), 5–19.

Manglik, A., Wicht, J. & Christensen, U.R., 2010. A dynamo model with double diffusive convection for Mercury's core, *Earth planet. Sci. Lett.,* **289,** 619–628.

Monville, R., Vidal, J., Cébron, D. & Schaeffer, N., 2019. Rotating double-diffusive convection in stably stratified planetary cores, *Geophys. J. Int.,* **219**(Suppl. 1), S195–S218.

Mound, J., Davies, C., Rost, S. & Aurnou, J., 2019. Regional stratification at the top of Earth's core due to core-mantle boundary heat flux variations, *Nat. Geosci.,* **12**(7), 575–580.

Nakagawa, T., 2011. Effect of a stably stratified layer near the outer boundary in numerical simulations of a magnetohydrodynamic dynamo in a rotating spherical shell and its implications for Earth's core, *Phys. Earth planet. Inter.,* **187,** 342–352.

Nakagawa, T., 2015. An implication for the origin of stratification below the core-mantle boundary region in numerical dynamo simulations in a rotating spherical shell, *Phys. Earth planet. Inter.,* **247,** 94–104.

Ohta, K., Kuwayama, Y., Hirose, K., Shimizu, K. & Ohishi, Y., 2016. Experimental determination of the electrical resistivity of iron at Earth's core conditions, *Nature,* **534**(7605), 95–98.

Olson, P., Landeau, M. & Reynolds, E., 2017. Dynamo tests for stratification below the core-mantle boundary, *Phys. Earth planet. Inter.,* **271,** 1–18.

Pozzo, M., Davies, C., Gubbins, D. & Alfè, D., 2012. Thermal and electrical conductivity of iron at Earth's core conditions, *Nature,* **485,** 355–358.

Pozzo, M., Davies, C., Gubbins, D. & Alfè, D., 2013. Transport properties for liquid silicon-oxygen-iron mixtures at Earth's core conditions, *Phys. Rev. B,* **87**(1), 014110.

Radko, T., 2013. *Double-Diffusive Convection,* Cambridge Univ. Press.

Rieutord, M., 1995. Inertial modes in the liquid core of the Earth, *Phys. Earth planet. Inter.,* **91,** 41–46.

Rogers, T.M. & Glatzmaier, G.A., 2005. Penetrative convection within the anelastic approximation, *Astrophys. J.*, **620,** 432–441.

Schaeffer, N., 2013. Efficient spherical harmonic transforms aimed at pseudospectral numerical simulations, *Geochem., Geophys., Geosyst.,* **14,** 751–758.

Schaeffer, N., Jault, D., Cardin, P. & Drouard, M., 2012. On the reflection of Alfvén waves and its implication for Earth's core modelling, *Geophys. J. Int.,* **191**(2), 508–516.

Schaeffer, N., Jault, D., Nataf, H.-C. & Fournier, A., 2017. Turbulent geodynamo simulations: a leap towards Earth's core, *Geophys. J. Int.,* **211**(1), 1–29.

Schwaiger, T., Gastine, T. & Aubert, J., 2019. Force balance in numerical geodynamo simulations: a systematic study, *Geophys. J. Int.,* **219,** S101–S114.

Silva, L., Mather, J.F. & Simitev, R.D., 2019. The onset of thermo-compositional convection in rotating spherical shells, *Geophys. Astrophys. Fluid Dyn.,* **113**(4), 377–404.

Souriau, A. & Poupinet, G., 1991. The velocity profile at the base of the liquid core from PKP(BC+Cdiff) data: an argument in favour of radial inhomogeneity, *Geophys. Res. Lett.,* **18,** 2023–2026.

Stacey, F.D. & Loper, D.E., 2007. A revised estimate of the conductivity of iron alloy at high pressure and implications for the core energy balance, *Phys. Earth planet. Inter.,* **161,** 13–18.

Stanley, S. & Mohammadi, A., 2008. Effects of an outer thin stably stratified layer on planetary dynamos, *Phys. Earth planet. Inter.,* **168,** 179–190.

Takahashi, F., Shimizu, H. & Tsunakawa, H., 2019. Mercury's anomalous magnetic field caused by a symmetry-breaking self-regulating dynamo, *Nat. Commun.,* **10,** 208.

Downloaded from https://academic.oup.com/gji/article-abstract/222/2/1433/5841194 by Biblio Planets user on 23 June 2020

Takehiro, S.-I., 2015. Penetration of Alfvén waves into an upper stably-stratified layer excited by magnetoconvection in rotating spherical shells, *Phys. Earth planet. Inter.,* **241,** 37–43.

Takehiro, S.-I. & Lister, J.R., 2001. Penetration of columnar convection into an outer stably stratified layer in rapidly rotating spherical fluid shells, *Earth planet. Sci. Lett.,* **187,** 357–366.

Takehiro, S.-I. & Sasaki, Y., 2018a. Penetration of steady fluid motions into an outer stable layer excited by MHD thermal convection in rotating spherical shells, *Phys. Earth planet. Inter.,* **276,** 258–264.

Takehiro, S.-I. & Sasaki, Y., 2018b. On destruction of a thermally stable layer by compositional convection in the Earth's outer core, *Front. Earth Sci.,* **6,** 192.

Tanaka, S., 2007. Possibility of a low P-wave velocity layer in the outermost core from global SmKS waveforms, *Earth planet. Sci. Lett.,* **259**(3-4), 486–499.

Tang, V., Zhao, L. & Hung, S.-H., 2015. Seismological evidence for a non-monotonic velocity gradient in the topmost outer core, *Sci. Rep.,* **5,** 8613.

Tilgner, A. & Busse, F.H., 1997. Finite-amplitude convection in rotating spherical fluid shells, *J. Fluid Mech.,* **332,** 359–376.

Vidal, J. & Schaeffer, N., 2015. Quasi-geostrophic modes in the Earth's fluid core with an outer stably stratified layer, *Geophys. J. Int.,* **202**(3), 2182–2193.

Wicht, J., 2002. Inner-core conductivity in numerical dynamo simulations, *Phys. Earth planet. Inter.,* **132,** 281–302.

Yadav, R.K., Gastine, T., Christensen, U.R., Wolk, S.J. & Poppenhaeger, K., 2016. Approaching a realistic force balance in geodynamo simulations, *Proc. Natl. Acad. Sci.,* **113**(43), 12 065–12 070.

Yan, C. & Stanley, S., 2018. Sensitivity of the geomagnetic octupole to a stably stratified layer in the Earth's Core, *Geophys. Res. Lett.,* **45,** 11.

Zahn, J.-P., 1991. Convective penetration in stellar interiors, *A&A,* **252,** 179–188.

APPENDIX

Table A1. Table of model parameters and results. The distances $\mathcal{H}_s$ and $\mathcal{D}_p$ are expressed in kilometres. The total run time $t_{\rm run}$ is given in magnetic diffusion time. All simulations have assumed $Pr = 1$. The numerical simulations with an asterisk in the last column have been computed with the PARODY-JA code.

Pm	$\mathcal{H}_s$	N_m/Ω	Rm	Λ	$\bar{\ell}_s$	$\mathcal{D}_p$	AD/NAD	O/E	Z/NZ	FCF	χ^2	N_r	$\ell_{\max}$	$\alpha_{\rm map}$	$t_{\rm run}$
							$E = 10^{-3},\ Ra = 3 \times 10^5$								
15.00	200	0.94	366	7.5	7	200	0.03	1.34	0.12	6.25	39.4	49	85	–	5.40
							$E = 3 \times 10^{-4},\ Ra = 3 \times 10^6$								
5.00	0	–	252	15.0	–	–	0.49	2.14	0.31	4.89	8.6	65	106	0.86	1.12
5.00	155	4.35	225	11.2	15	131	1.94	3.53	0.50	2.07	5.6	81	106	–	1.60
5.00	200	0.82	248	13.6	13	200	0.61	2.42	0.33	4.43	7.5	81	106	–	1.15
5.00	200	0.95	246	13.9	13	200	0.68	2.18	0.32	4.08	6.3	65	106	–	1.11
5.00	200	4.35	214	12.4	14	161	2.56	3.41	0.48	1.78	5.6	81	106	–	2.14
5.00	290	0.82	240	13.9	12	290	0.74	2.57	0.31	3.92	6.3	81	106	–	1.50
5.00	290	1.37	229	12.9	13	270	1.11	3.37	0.31	3.24	5.7	81	106	–	2.03
5.00	290	4.35	202	12.7	13	179	3.01	3.88	0.52	1.62	6.9	97	106	–	1.36
5.00	290	7.35	196	12.7	13	129	3.30	4.33	0.55	1.54	8.0	129	106	–	1.31
5.00	290	13.75	189	12.7	13	92	4.02	3.56	0.56	1.39	7.8	145	106	–	1.71
5.00	290	23.24	186	12.6	13	69	4.28	4.22	0.63	1.41	9.4	145	106	–	1.12
5.00	290	43.47	183	12.1	13	48	4.45	4.03	0.94	1.44	10.9	193	106	–	1.13
							$E = 10^{-4},\ Ra = 4 \times 10^7$								
3.50	200	0.95	407	19.4	20	191	1.19	2.02	0.38	2.63	3.1	81	106	–	1.30
							$E = 3 \times 10^{-5},\ Ra = 10^8$								
2.50	0	–	302	17.9	–	–	1.31	1.53	0.19	3.65	3.0	81	106	0.91	1.12
2.50	200	0.47	288	16.1	25	193	1.86	1.51	0.17	2.80	1.8	81	106	0.91	1.05
2.50	200	0.82	292	12.4	26	191	3.53	2.00	0.29	1.58	3.3	81	106	0.91	1.08
2.50	200	1.64	282	11.5	27	161	6.10	2.73	0.42	1.20	8.0	81	106	0.91	1.04
							$E = 3 \times 10^{-5},\ Ra = 3 \times 10^8$								
1.00	0	–	234	7.6	–	–	2.59	1.59	0.24	1.87	1.7	81	128	–	1.00
1.00	200	1.64	213	6.9	34	188	9.29	2.50	0.51	1.04	11.4	81	128	–	1.29
1.00	200	5.20	205	6.3	35	87	16.35	2.77	0.74	0.86	18.8	81	128	–	1.03
2.50	0	–	555	23.2	–	–	1.54	1.58	0.28	2.19	1.4	81	128	0.91	1.04
2.50	53	3.29	550	18.1	36	47	3.08	1.98	0.43	1.56	3.6	81	128	0.91	1.09
2.50	53	5.20	543	17.1	41	45	3.85	2.35	0.53	1.31	5.6	145	128	0.97	1.13
2.50	87	0.82	546	22.8	31	83	1.70	1.59	0.30	2.12	1.5	81	128	0.91	1.03
2.50	87	1.64	548	19.9	34	81	2.47	1.90	0.34	1.76	2.4	81	128	0.91	1.18
2.50	87	2.85	535	18.2	38	79	3.91	2.25	0.53	1.40	5.5	81	128	–	0.82
2.50	87	5.20	533	17.4	40	62	5.35	2.40	0.53	1.12	7.5	97	128	0.93	1.38
2.50	87	9.00	522	17.6	39	39	6.82	2.21	0.46	1.02	8.5	161	128	0.97	1.01
2.50	87	16.43	517	18.1	37	27	7.70	2.17	0.40	0.97	9.0	161	128	0.97	1.10
2.50	155	0.47	541	23.3	29	155	1.63	1.73	0.30	2.25	1.8	81	128	0.91	1.10
2.50	155	0.82	535	22.4	31	149	2.07	1.71	0.29	2.02	1.7	81	128	0.91	1.05
2.50	155	1.64	527	18.9	34	144	4.16	2.35	0.53	1.39	5.9	81	128	–	1.17
2.50	155	2.85	516	18.5	36	111	6.00	2.49	0.60	1.14	8.7	81	128	0.91	1.16
2.50	155	5.20	503	18.7	36	75	8.12	2.56	0.58	1.01	10.9	145	128	0.96	1.00
2.50	155	28.46	487	18.5	35	25	10.95	2.22	0.52	0.85	13.0	145	133	0.97	1.15

Downloaded from https://academic.oup.com/gji/article-abstract/222/2/1433/5841194 by Biblio Planets user on 23 June 2020

Table A1. Continued

Pm	$\mathcal{H}_s$	N_m/Ω	Rm	Λ	$\bar{\ell}_s$	$\mathcal{D}_p$	AD/NAD	O/E	Z/NZ	FCF	χ^2	N_r	$\ell_{\max}$	α_{map}	t_{run}
2.50	200	0.26	536	24.2	30	200	1.62	1.66	0.27	2.31	1.6	81	128	0.91	1.07
2.50	200	0.82	526	21.5	31	193	2.41	1.89	0.34	1.90	2.4	81	128	0.91	1.06
2.50	200	0.95	528	20.2	31	192	2.86	1.96	0.36	1.73	3.0	81	133	0.91	1.40
2.50	200	1.64	519	18.7	33	182	4.48	2.90	0.59	1.33	7.4	81	128	–	1.51
2.50	200	5.20	489	18.4	35	88	9.87	2.89	0.65	0.93	13.6	145	170	0.97	1.03
2.50	200	8.22	485	18.4	36	64	11.80	2.60	0.59	0.86	14.6	145	128	–	1.10
2.50	200	16.43	477	17.9	36	40	12.28	2.68	0.57	0.79	15.3	145	128	0.97	1.19
2.50	200	51.96	465	17.5	35	19	12.97	2.16	0.57	0.79	15.0	257	170	0.98	1.03
2.50	290	0.26	524	24.3	28	290	1.61	1.60	0.28	2.38	1.6	81	128	0.91	1.07
2.50	290	0.82	515	19.6	30	281	3.10	2.14	0.39	1.67	3.6	81	128	0.91	1.44
2.50	290	4.35	462	17.9	32	119	13.94	2.86	0.66	0.79	17.2	81	128	0.91	1.08
2.50	290	16.43	447	16.5	37	47	17.04	2.98	0.76	0.70	20.4	145	128	0.97	1.10
4.33	0	–	935	46.2	–	–	1.23	1.49	0.27	2.40	1.5	160	133	–	0.48*
4.33	87	2.00	908	38.0	–	79	2.36	1.90	0.40	1.83	2.7	160	133	–	0.55*
4.33	155	1.00	891	42.7	–	147	1.85	1.76	0.29	2.04	1.6	160	133	–	0.54*
4.33	200	0.82	888	43.1	–	192	1.68	1.71	0.27	2.35	1.7	160	133	–	0.71*
4.33	200	0.95	879	41.4	–	192	2.08	1.86	0.32	1.98	2.1	160	133	–	0.73*
4.33	200	1.64	867	37.0	–	174	3.97	2.61	0.51	1.36	6.0	160	133	–	0.68*
4.33	290	0.82	863	40.2	–	278	2.23	2.01	0.30	1.90	2.2	160	133	–	0.74*
4.33	290	0.95	858	38.0	–	278	2.64	2.37	0.37	1.76	3.4	160	133	–	0.67*
4.33	290	1.64	820	36.9	–	224	6.99	2.64	0.48	1.02	9.4	160	133	–	0.64*
$E = 3 \times 10^{-5},\ Ra = 10^9$															
1.44	0	–	617	17.3	–	–	1.88	2.34	0.58	1.74	3.9	97	170	0.93	1.09
1.44	155	0.87	596	17.2	33	150	2.33	2.31	0.64	1.71	4.6	97	170	0.93	1.07
1.44	155	1.73	583	16.2	36	148	3.79	2.73	0.68	1.49	6.9	97	170	–	1.47
1.44	200	0.87	587	17.4	33	194	2.70	2.35	0.60	1.67	4.8	97	170	0.93	1.08
1.44	200	1.73	578	15.5	36	191	4.57	3.15	0.78	1.33	8.9	97	170	0.93	1.22
1.44	290	1.73	561	14.9	34	275	5.67	3.93	0.81	1.18	11.5	97	170	0.97	1.17
$E = 10^{-5},\ Ra = 2 \times 10^9$															
1.20	0	–	442	15.7	–	–	2.48	1.52	0.19	1.85	1.2	129	192	0.96	1.05
1.20	155	0.47	429	15.3	43	151	3.57	1.53	0.20	1.57	2.3	129	192	0.96	1.08
1.20	200	0.95	415	13.8	41	189	8.44	2.00	0.33	1.07	8.8	129	192	0.96	1.01
$E = 3 \times 10^{-6},\ Ra = 10^{10}$															
0.80	0	–	387	13.1	–	–	3.29	1.40	0.12	1.71	1.9	161	256	0.97	0.67
0.80	155	0.47	375	12.0	55	150	6.30	1.31	0.17	1.22	5.0	161	256	0.97	0.66
0.80	200	0.95	388	10.0	59	152	10.43	3.11	0.31	0.92	12.5	193	256	0.98	0.60
$E = 3 \times 10^{-6},\ Ra = 3 \times 10^{10}$															
0.80	155	1.64	651	17.6	65	110	10.78	2.13	0.42	0.85	12.2	193	288	0.98	0.51
$E = 10^{-6},\ Ra = 9 \times 10^{10}$															
0.50	200	0.95	461	9.1	74	152	5.09	6.94	0.50	1.00	13.6	321	426	0.99	0.23

Downloaded from https://academic.oup.com/gji/article-abstract/222/2/1433/5841194 by Biblio Planets user on 23 June 2020